JCI The Journal of Clinical Investigation

Tumor restriction by type I collagen opposes tumor-promoting effects of cancer-associated fibroblasts

Sonakshi Bhattacharjee, Florian Hamberger, Aashreya Ravichandra, Maximilian Miller, Ajay Nair, Silvia Affo, Aveline Filliol, LiKang Chin, Thomas M. Savage, Deqi Yin, Naita Maren Wirsik, Adam Mehal, Nicholas Arpaia, Ekihiro Seki, Matthias Mack, Di Zhu, Peter A. Sims, Raghu Kalluri, Ben Z. Stanger, Kenneth P. Olive, Thomas Schmidt, Rebecca G. Wells, Ingmar Mederacke, Robert F. Schwabe

J Clin Invest. 2021;131(11):e146987. https://doi.org/10.1172/JCI146987.

Research Article | Hepatology | Oncology

Graphical abstract

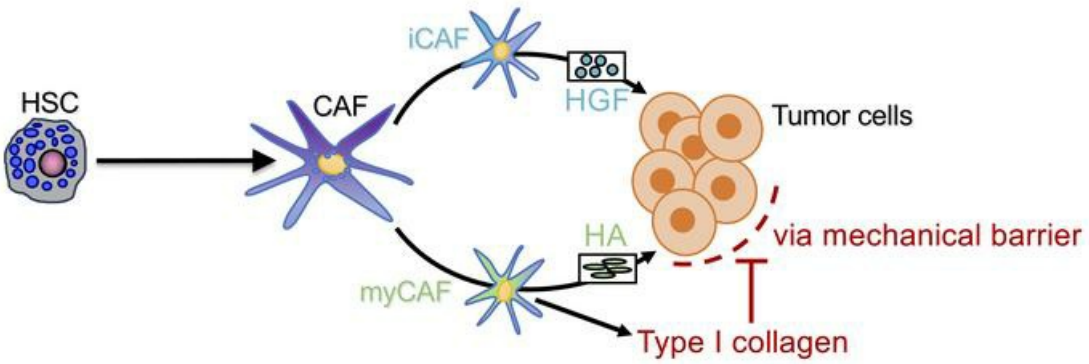

Tumor restriction by type I collagen opposes tumor-promoting effects of cancer-associated fibroblasts

Sonakshi Bhattacharjee,[1] Florian Hamberger,[2] Aashreya Ravichandra,[1] Maximilian Miller,[3] Ajay Nair,[1] Silvia Affo,[1] Aveline Filliol,[1] LiKang Chin,[4] Thomas M. Savage,[5] Deqi Yin,[1] Naita Maren Wirsik,[6] Adam Mehal,[1] Nicholas Arpaia,[5,7] Ekihiro Seki,[8] Matthias Mack,[9] Di Zhu,[10] Peter A. Sims,[11] Raghu Kalluri,[12] Ben Z. Stanger,[4] Kenneth P. Olive,[1] Thomas Schmidt,[6] Rebecca G. Wells,[4] Ingmar Mederacke,[2] and Robert F. Schwabe[1,13]

[1]Department of Medicine, Columbia University, New York, New York, USA. [2]Department of Gastroenterology, Hepatology, and Endocrinology, Hannover Medical School, Hanover, Germany. [3]Department of Biochemistry and Microbiology, Rutgers University, New Brunswick, New Jersey, USA. [4]Perelman School of Medicine, University of Pennsylvania, Philadelphia, Pennsylvania, USA. [5]Department of Microbiology and Immunology, Columbia University, New York, New York, USA. [6]Department of General, Visceral and Transplantation Surgery, University Hospital Heidelberg, Heidelberg University, Heidelberg, Germany. [7]Herbert Irving Comprehensive Cancer Center, Columbia University, New York, New York, USA. [8]Department of Medicine, Division of Digestive and Liver Diseases, Cedars-Sinai Medical Center, Los Angeles, California, USA. [9]Department of Nephrology, University Hospital Regensburg, Regensburg, Germany. [10]Department of Pharmacology, Minhang Hospital and School of Pharmacy, Fudan University, Shanghai, China. [11]Department of Systems Biology, Columbia University, New York, New York, USA. [12]Department of Cancer Biology, The University of Texas MD Anderson Cancer Center, Houston, Texas, USA. [13]Institute of Human Nutrition, Columbia University, New York, New York, USA.

Cancer-associated fibroblasts (CAF) may exert tumor-promoting and tumor-suppressive functions, but the mechanisms underlying these opposing effects remain elusive. Here, we sought to understand these potentially opposing functions by interrogating functional relationships among CAF subtypes, their mediators, desmoplasia, and tumor growth in a wide range of tumor types metastasizing to the liver, the most common organ site for metastasis. Depletion of hepatic stellate cells (HSC), which represented the main source of CAF in mice and patients in our study, or depletion of all CAF decreased tumor growth and mortality in desmoplastic colorectal and pancreatic metastasis but not in nondesmoplastic metastatic tumors. Single-cell RNA-Seq in conjunction with CellPhoneDB ligand-receptor analysis, as well as studies in immune cell–depleted and HSC-selective knockout mice, uncovered direct CAF-tumor interactions as a tumor-promoting mechanism, mediated by myofibroblastic CAF–secreted (myCAF-secreted) hyaluronan and inflammatory CAF–secreted (iCAF-secreted) HGF. These effects were opposed by myCAF-expressed type I collagen, which suppressed tumor growth by mechanically restraining tumor spread, overriding its own stiffness-induced mechanosignals. In summary, mechanical restriction by type I collagen opposes the overall tumor-promoting effects of CAF, thus providing a mechanistic explanation for their dual functions in cancer. Therapeutic targeting of tumor-promoting CAF mediators while preserving type I collagen may convert CAF from tumor promoting to tumor restricting.

Introduction

Metastasis is the main cause of mortality in the majority of patients with tumors, and the liver represents the main organ site for metastatic seeding and growth (1–4). Pancreatic ductal adenocarcinoma (PDAC) and colorectal cancer (CRC) are among the most common tumors that metastasize to the liver due to their anatomical link via the portal vein (2, 5, 6). Of note, therapeutic approaches for liver metastasis are clinically significant, as surgical removal of single CRC lesions can be curative (7, 8). However, the majority of metastases are not amenable to surgical interventions, and current therapies focus largely on targeting the tumor without considering the complex hepatic microenvironment in which tumors grow. Moreover, its central metabolic role with abundant nutrients and growth factors render the liver a fertile soil for metastatic tumor growth and amenable to treatments targeting this growth-promoting tumor microenvironment. The stroma arising from PDAC or CRC metastasis comprises a highly complex ecosystem of endothelial cells, immune cells, and cancer-associated fibroblasts (CAF) (9–11). The latter make up the majority of the desmoplastic stroma and have been shown to promote the growth of primary tumors (12–16). However, recent studies in PDAC in vivo models have demonstrated a tumor-restricting and survival-promoting roles for CAF (17, 18). Even though CAF are thought to mainly be tumor promoting in primary liver cancer, metastatic lesions are commonly encased by dense CAF and fibrotic tissue similar to bacterial abscesses or parasitic lesions, suggesting that CAF and desmoplasia may serve to restrain tumor expansion akin to its functions in infectious processes (19, 20). Single-cell RNA-Seq (scRNA-Seq) studies have revealed significant heterogeneity within pancreatic CAF populations, suggesting that more complex interactions are at play, where specific subsets may interact with tumor cells and

Conflict of interest: The authors have declared that no conflict of interest exists.

Submitted: December 23, 2020; **Accepted:** April 8, 2021; **Published:** June 1, 2021.
Reference information: *J Clin Invest*. 2021;131(11):e146987.
https://doi.org/10.1172/JCI146987.

the immune system distinctly from others (21–23). CAF have also been shown to have different precursors based on tumor localization — including stem cells, resident fibroblasts, and the bone marrow (12, 15, 24). Ontogeny, diversity, or function of CAF in liver metastasis remain largely unknown, despite the extent of the underlying clinical problem. While the premetastatic niche has been carefully investigated, in particular in PDAC (25), it remains unclear whether and how CAF promote or restrict further growth of seeded tumor cells. In this regard, growth factors such as hepatocyte growth factor (HGF), which is abundantly expressed by hepatic stellate cells (HSC), the main fibrogenic cell type of the liver (26), may contribute to tumor growth. Likewise, CAF-derived extracellular matrix (ECM) such as collagen and associated stiffness may enhance growth via the activation of mechanosensitive pathways (27–29) or restrict lesions akin to infectious processes in the liver. Finally, CAF can promote an immunosuppressive environment via T cell exclusion and negative modulation of T cell activation, thus promoting tumor growth (12, 14, 19).

Using genetic tracing in combination with scRNA-Seq as well as genetic depletion through Cre-lox–mediated deletion approaches, we demonstrate that CAF arise primarily from resident HSC. HSC-CAF primarily promote the growth of desmoplastic liver metastasis through hyaluronan (HA) and HGF, mediated by direct CAF-tumor interactions and independently of adaptive immunity, whereas type I collagen secreted by HSC-CAF restricts metastatic growth.

Results

Metastasis-associated CAF are primarily HSC derived. To determine CAF ontogeny during liver metastasis, we subjected triple transgenic mice expressing LratCre-induced TdTomato, faithfully marking the HSC lineage (26), and Col1a1-GFP, marking all collagen-producing fibroblasts to hemispleen injection of different tumor cells. PDAC and CRC cell lines Pan02 and CMT93 induced desmoplastic metastasis, as confirmed by Col1a1-GFP expression, α-smooth muscle actin (αSMA) IHC, and Sirius red staining, whereas breast and melanoma cell lines EO771 and B16F10 resulted in nondesmoplastic metastatic growth (Figure 1A). In all metastasis models, we observed over 90% colocalization of Col1a1-GFP$^+$ CAF with Lrat-TdTomato$^+$ HSC but detected considerably lower numbers of CAF in nondesmoplastic tumors induced by EO771 and B16F10 cells (Figure 1B). Moreover, we found that HSC marker desmin colocalized with LratCre-induced TdTomato, confirming the validity of our approach (Supplemental Figure 1A; supplemental material available online with this article; https://doi.org/10.1172/JCI146987DS1), and showed that Col1a1-producing CAF were only present within CK19$^+$ tumor areas (Supplemental Figure 1B). In order to verify that liver metastasis in CRC is desmoplastic and contains αSMA$^+$ CAF, we stained liver metastasis sections in a cohort of 100 patients for αSMA. All patients had αSMA$^+$ CAF present inside tumors but to varying degrees. In paired tumor and nontumor patient-matched samples, αSMA expression was significantly higher in tumor area compared with that in nontumor tissue (Figure 1C). To confirm CAF identity by a second approach in vivo, we next performed scRNA-Seq in CAF-enriched fractions of the desmoplastic PDAC (Pan02, KPCY) and CRC (CMT93) models (Figure 2A and Supplemental Figure 2A). 80%–91% of CAF showed strong expression of an HSC signature that included HSC markers *Lrat*, *Lum*, and *Pdgfrb*, while a second cell cluster constituted the remaining 9%–19% expressed mesothelial markers *Msln*, *Upk1b*, and *Up3kb*, which are expressed in portal fibroblasts (PFs) (30) (Figure 2A). These findings were confirmed in 6 patients with human liver metastasis of CRC and 1 patient with intestinal neuroendocrine tumor (NET), which is often desmoplastic and frequently metastasizes to the liver (31, 32). In human liver metastasis, 90%–100% of CAF expressed an HSC signature, including *PDGFRB*, *GEM*, and *FRZB* (Figure 2A and Supplemental Figure 3, A–C). In contrast, none of the human CAF expressed a PF signature, including PF markers *MSLN*, *UPK1B*, and *UPK3B*. Together, these findings extend those of previous studies that showed accumulation of HSC-enriched genes or signatures in CRC and PDAC liver metastasis but did not investigate the relative contribution of HSC to the CAF pool (33–35).

Metastasis-associated CAF segregate into myCAF, iCAF, and mesCAF populations. In addition to differences in CAF ontogeny as modulator of CAF biology, recent scRNA-Seq studies have provided evidence for functional CAF diversity. A modified liver CAF scRNA-Seq signature, based on recent scRNA-Seq signatures for CAF subtypes in pancreatic and breast cancer (22, 23), segregated CAF into 3 distinct subtypes (Supplemental Figure 2, B–E, and Supplemental Table 1). The majority of CAF in liver metastasis were classified as myofibroblastic CAF (myCAF) expressing high levels of *Acta2* and several collagen isoforms (Figure 2B and Supplemental Figure 2, B–E). A second CAF subset was defined as growth factor and inflammatory gene–expressing CAF (iCAF), representing CAF expressing lower levels of activation markers and high levels of growth factors (Figure 2B). The main characteristic of the PF/mesothelial CAF (PF/mesCAF) population was the expression of mesothelial markers, with lower expression of myofibroblast markers, cytokines, and growth factors than the myCAF and iCAF populations (Supplemental Figure 2, C and E). To confirm the presence of these populations in situ, we analyzed CAF based on expression of both Lrat-TdTomato and Col-GFP, clearly segregating TdTomato$^+$ HSC-CAF into Col-GFP^{hi} cells, representing myCAF, and Col-GFP^{lo} cells, representing iCAF. There was no evidence for selective accumulation of either cell type in specific tumor regions (Supplemental Figure 1C). Finally, the presence of iCAF and myCAF populations was confirmed in human CRC and intestinal NET liver metastasis while mesCAF were not detected (Figure 2B and Supplemental Figure 3, E–H).

CAF promote proliferation, progression, and lethality in desmoplastic liver metastasis. After classifying origin and subpopulations of metastasis-associated CAF by tracing and single-cell transcriptomics, we next sought to understand their role in liver metastasis. Given that HSC-CAF represented the majority of CAF in all models, our first approach to interrogate their functions was genetic depletion in triple transgenic mice coexpressing LratCre, Cre reporter lox-stop-lox TdTomato, and Cre-inducible diphtheria toxin receptor (iDTR), allowing us to monitor depletion of CAF-HSC via TdTomato in LratCre$^+$iDTR$^+$ mice and their LratCre$^+$iDTR$^-$ littermates. Following administration of diphtheria toxin (DT), we depleted up to 97% of HSC-CAF in the Pan02 and CMT93 metastasis models, shown through mRNA as well as TdTomato signal (Figure 3A and Supplemental Figure 4, A and

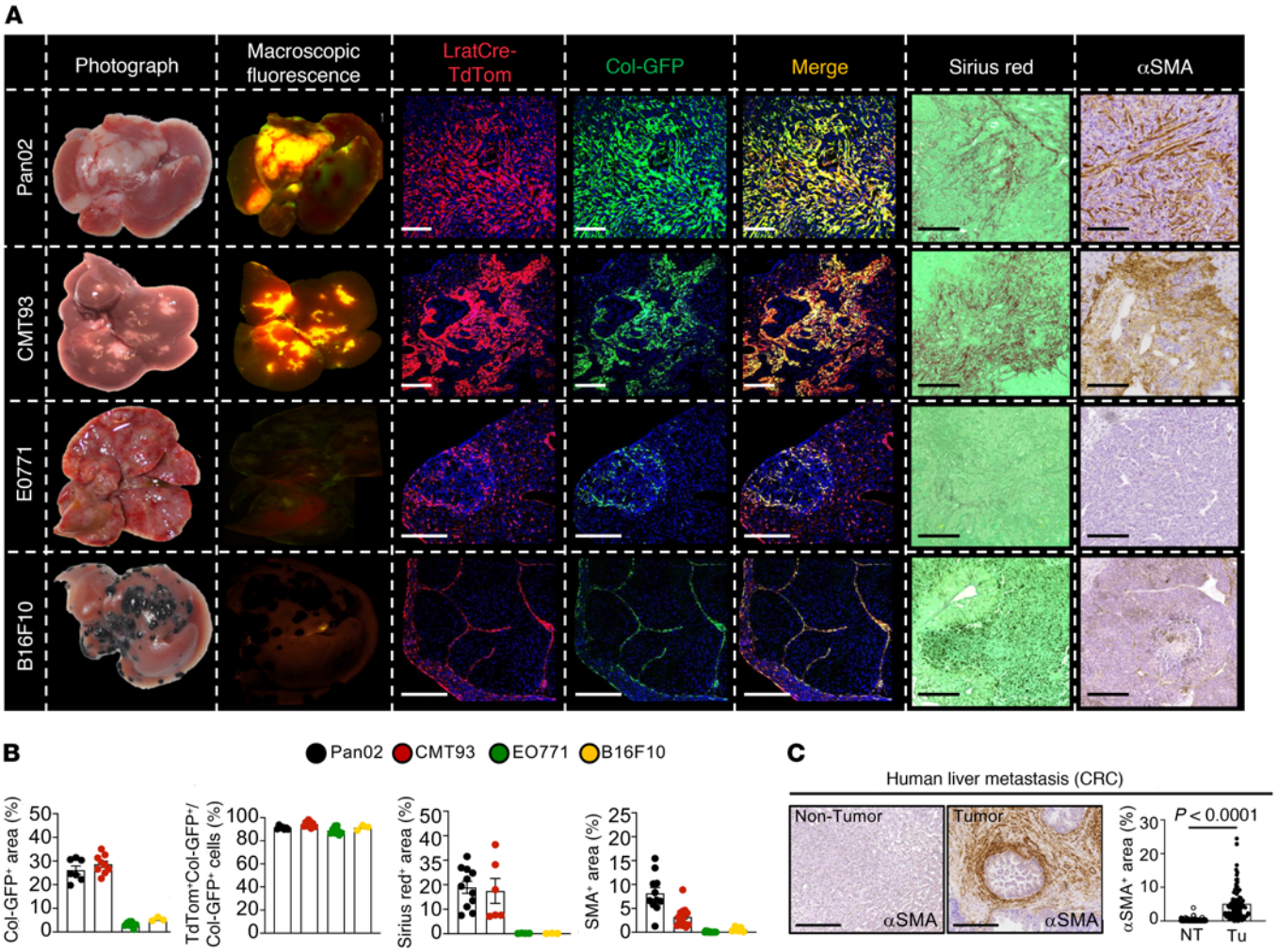

Figure 1. CAF ontogeny in mouse and human liver metastasis. (**A**) Tumor images and their macroscopic fluorescence of LratCre-TdTom and collagen1a1-GFP; confocal microscopy of LratCre-TdTom, collagen1a1-GFP (Col-GFP), Sirius red, and αSMA IHC in Pan02, CMT93, EO771, and B16F10 liver metastasis. Scale bars: 100 μm. (**B**) Quantification of data in **A**. Data are shown as the mean ± SEM; *n* = 3–9 mice/cell line. (**C**) Representative IHC and quantifications of αSMA in human CRC liver metastasis (*n* = 100). NT, nontumor; Tu, tumor. Scale bars: 100 μm. Data are shown as the mean ± SEM; paired *t* test.

B), accompanied by reduced fibrosis, as shown by a decrease in *Col1a1* and Sirius Red staining (Figure 3B). Notably, the dose of DT employed did not result in a loss of body weight in animals (Supplemental Figure 4C). Depletion of HSC-CAF in desmoplastic metastasis models resulted in a profound reduction in the liver-to-body weight ratio, an indirect measure of hepatic tumor mass, in PDAC and CRC metastasis models as well the tumor area, determined by immunohistochemical staining for CK19 or GFP (Figure 3C). In contrast, HSC-CAF depletion in nondesmoplastic B16F10 and EO771 models did not alter liver-to-body weight ratios and tumor area (Figure 3C). Survival studies demonstrated a profound benefit for all animals after CAF depletion via LratCre$^+$iDTR (Figure 3D). As a second CAF depletion strategy, targeting proliferating CAF, we used αSMA–thymidine kinase–transgenic (αSMA-TK–transgenic) mice, in which ganciclovir led to CAF depletion and reduction of fibrosis with similar efficacy as observed for the LratCre-iDTR model (Figure 4, A and B, and Supplemental Figure 4, D and E). Similar to HSC-CAF depletion, CAF depletion via αSMA-TK achieved highly significant tumor reduction in 2 PDAC (Pan02, KPCY) models and 1 CRC (CMT93) model, as evidenced by decreased liver-to-body weight ratio and tumor area (Figure 4C and Supplemental Figure 4F). Survival studies also demonstrated a profound benefit for all animals after CAF depletion, even via αSMA-TK (Figure 4D). To mimic clinically relevant scenarios, we additionally depleted CAF at late time points after tumor induction (Figure 5A). Surprisingly even with depletion at day 10 onward in our 14-day model, in both Lrat-iDTR and αSMA-TK animals, tumors depleted of CAF were significantly smaller (Figure 5, B and C, and Supplemental Figure 5A). We also observed a significant survival benefit in day 13 onward CAF-depleted mice, albeit with a smaller effect on size than when we consistently depleted CAF throughout (Figure 5D). CT imaging revealed that CAF depletion almost halted tumor progression but did not shrink tumors that had already developed (Figure 5E). Further, IHC revealed a reduction of Ki67$^+$ proliferating tumor cells in both models, indicating that CAF promote tumor cell proliferation and their survival (Figure 6A and Supplemental Figure 5B). Particularly, we demonstrate that at this time point that almost all Ki67$^+$ cells are CK19$^+$ tumor

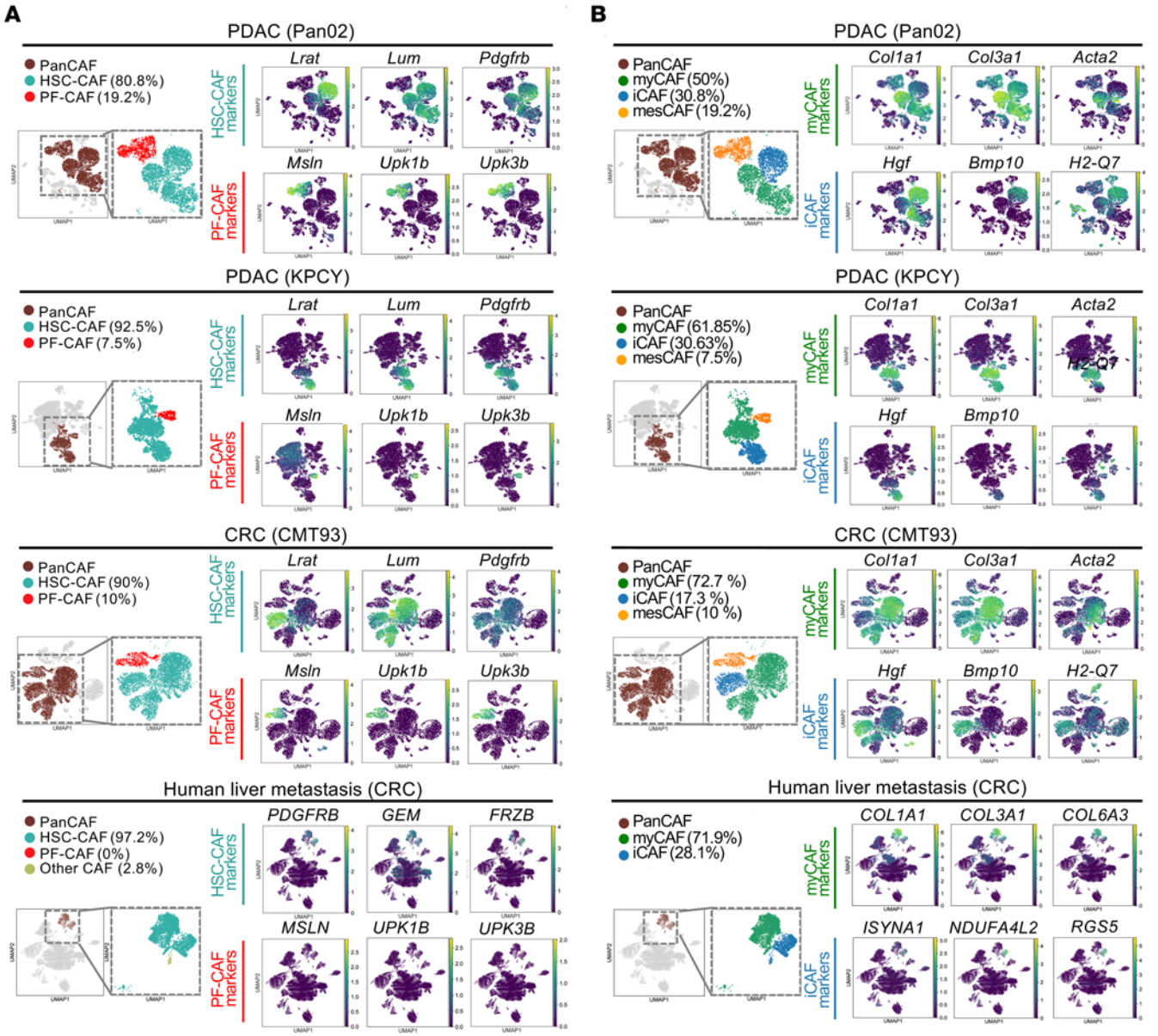

Figure 2. CAF subpopulations in mouse and human liver metastasis. (**A**) UMAPs of scRNA-Seq of murine PDAC and CRC liver metastasis (n = 1 each) and human CRC metastasis (n = 6), displaying HSC and PF as a percentage of panCAF; murine HSC markers *Lrat*, *Lum*, and *Pdgfrb*; murine PF marker *Msln*, *Upk1b*, and *Upk3b;* human HSC markers *PDGFRB*, *GEM*, and *FRZB*; and human PF markers *MSLN*, *UPK1B*, and *UPK3B*. (**B**) UMAPs showing percentages and markers of myCAF, iCAF, and mesCAF subpopulations for murine PDAC models Pan02 and KPCY (n = 1 each), murine CRC model CMT93 (n = 1) and human CRC liver metastasis (n = 6).

cells and not TdTomato$^+$ CAF (Supplemental Figure 5C). Notably, no significant differences were observed in cleaved caspase-3 staining between CAF-depleted mice and undepleted controls (Supplemental Figure 5, D and E).

Direct CAF-tumor interactions promote tumor growth, independently of adaptive immunity. In order to understand how CAF promote tumor growth, we analyzed ligand-receptor interactions between different cell types in our mouse and human scRNA-Seq data by CellPhoneDB (36) (Supplemental Table 3). This analysis revealed that tumor cells interacted most intensely with panCAF, followed by endothelial cells, Kupffer cells, and macrophages (Figure 6B). However, CAF also had numerous interactions with other cell types, including T cells, hepatocytes, and endothelial cells, suggesting that direct CAF-tumor interactions, interactions with other cell types, or both could mediate the tumor-promoting effect of CAF (Figure 6B). The strong interaction between HSC and endothelial cells, as observed in our CellPhoneDB analysis, is well recognized for normal and diseased liver (37). However, CAF depletion did not affect angiogenesis, as demonstrated by qPCR for endothelial cell makers *Pecam* (encoding CD31) and *Kdr* (encoding VEGFR2), suggesting that CAF affect metastatic tumor growth through other cell types (Supplemental Figure 5F). Next, we addressed the possibility that CAF and CAF-produced ECM may alter antitumor immunity via immune exclusion, as suggested by previous studies, (12, 14, 15, 19); we compared the immune landscape between CAF-depleted and nondepleted control tumors by

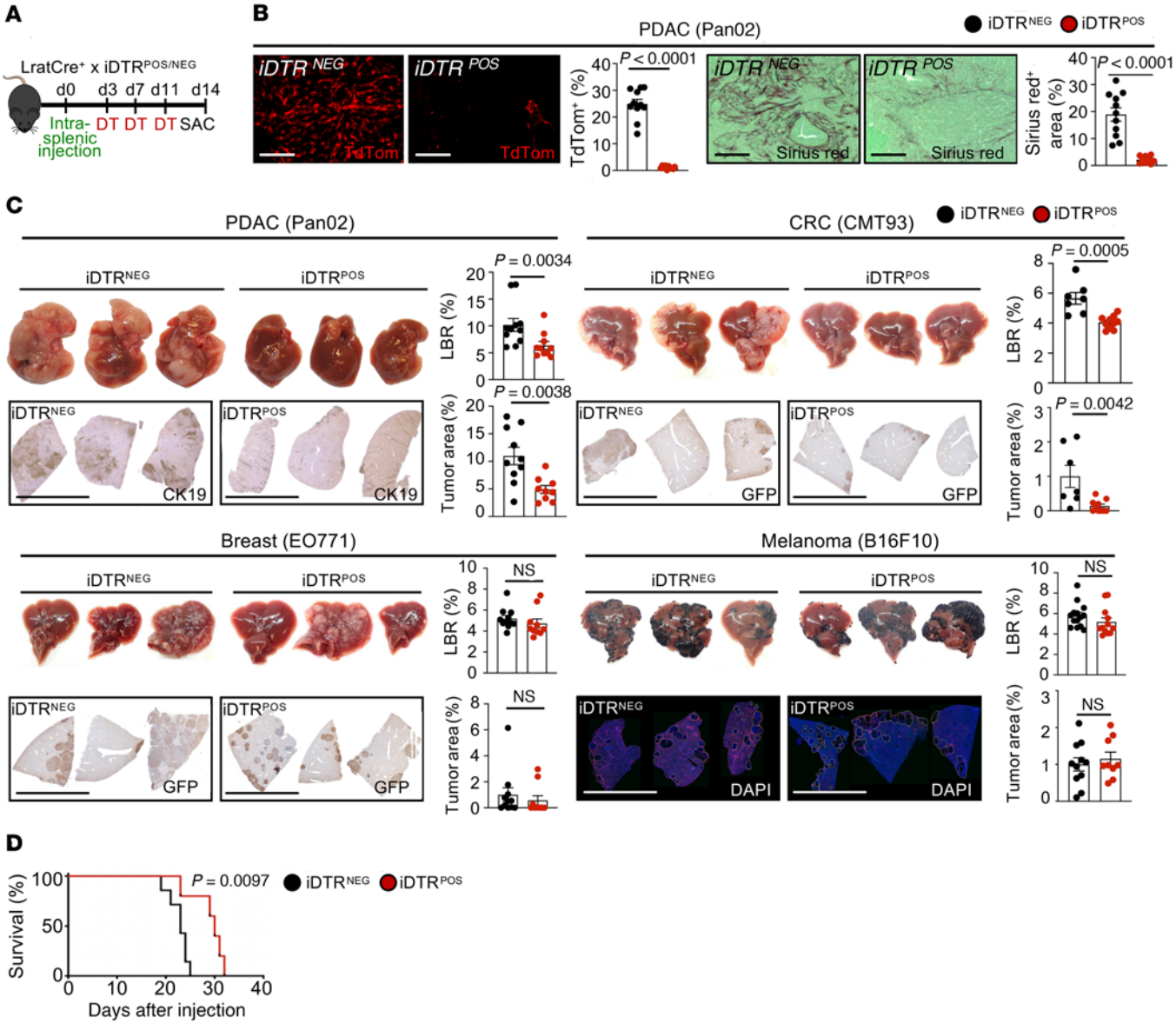

Figure 3. HSC-derived CAF promote desmoplastic tumor growth and mortality. (**A** and **B**) HSC-CAF depletion via DT injection (0.5 ng/g BW) in LratCre$^+$ TdTom$^+$iDTR$^+$ or LratCre$^+$TdTom$^+$iDTR$^-$ littermates (**B**) reduces TdTom expression and Sirius red in tumors. Scale bars: 100 μm. (**C**) Representative macroscopic and IHC images of liver and liver-to-body weight ratio (LBR) and tumor area quantifications (n = 7–15 mice/group), showing effects of HSC-CAF depletion on desmoplastic (Pan02, CMT93) but not on nondesmoplastic (EO771, B16F10) liver metastasis. Scale bars: 1 cm. (**D**) Survival studies in iDTR mice injected with DT until death (n = 5–8 mice/group for each model). Statistics were done by 2-tailed unpaired t test or Mann Whitney U (**B** and **C**) or Mantel-Cox test (**D**). Data are shown as the mean ± SEM.

flow cytometry. We did not observe significant changes in myeloid or lymphoid populations apart from a reduction of Foxp3$^+$ Tregs upon CAF depletion (Supplemental Figure 6, A and B) To directly assess if CAF depletion resulted in increased access to antitumor CD8$^+$ cells and thus reduced tumors, we depleted CD8$^+$ cells or used isotype controls in CAF-depleted and nondepleted control mice. To additionally exclude the possibility of CD4$^+$ cells playing a role or compensating during CD8$^+$ cell depletion, we depleted both CD4$^+$ and CD8$^+$ cells in the same setting. In CD8$^+$ or both CD4$^+$/CD8$^+$-depleted mice, we still observed a drastic reduction of tumor burden by CAF depletion that was similar in extent to all previous CAF depletion experiments, demonstrating that CAF may promote tumor growth through direct interactions independent of antitumor immunity (Figure 7A and Supplemental Figure 6, C and D). Finally, 3D in vitro coculture or subcutaneous coinjection of HSC with Pan02 cells into *RAG2*$^{-/-}$ mice, deficient in T and B cells, strongly augmented tumor size, demonstrating direct CAF-tumor interaction as a predominant driver of tumor growth, independent of immune cells, in line with our initial CellPhoneDB analysis (Figure 7, B and C). Additionally, CellPhoneDB analysis determined HSC-CAF, and not PF-CAF or other-CAF, as the main interaction partner for tumor cells for both murine and human liver metastasis (Figure 7D). A list of the common top interaction partners for all 3 murine cell lines are provided in Supplemental Table 2.

myCAF-expressed type I collagen restricts desmoplastic tumor growth. To determine factors mediating tumor-promoting inter-

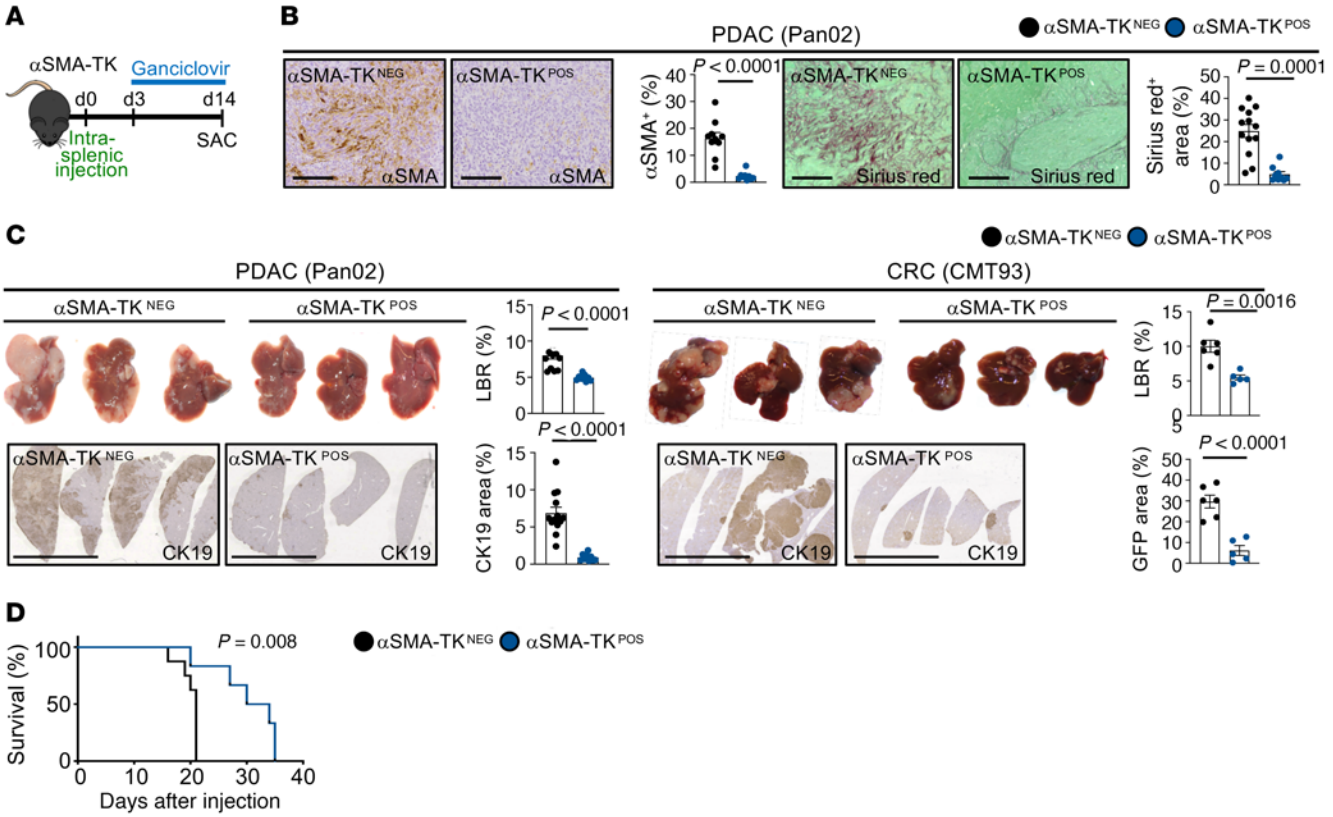

Figure 4. αSMA⁺ CAF promote desmoplastic tumor growth and mortality. (**A–C**) CAF depletion in αSMA-TK mice, injected daily from day 3 after surgery with ganciclovir (10 mg/kg) (**B**) reduces αSMA IHC (n = 9–10 mice/group) and Sirius red (n = 9–13 mice/group). Scale bars: 100 μm. (**C**) Representative macroscopic and IHC images of liver and liver-to-body weight ratio (LBR) and tumor area quantification, showing the effects of CAF depletion on Pan02 and CMT93 liver metastasis (n = 5–13 mice/group). Scale bars: 1 cm. (**D**) Survival studies in αSMA-TK mice injected with ganciclovir until death (n = 5–8 mice/group for each model). Statistics were done by 2-tailed unpaired t test or Mann Whitney U (**B** and **C**) or Mantel-Cox test (**D**). Data are shown as the mean ± SEM.

actions between CAF and tumor cells, we investigated strongly upregulated genes in CAF in our scRNA-Seq data as well as in bulk RNA-Seq data from highly pure HSC-CAF isolates. Among the top upregulated genes were several collagens as well as other ECM-associated genes (Supplemental Figure 7A). scRNA-Seq analysis revealed high expression of *Col1a1* in myCAF compared with iCAF or mesCAF clusters (Figure 8A). As previous studies in other models have demonstrated an effect of mechanosensitive signals, stiffness, and desmoplasia on tumor growth (27–29), we first investigated the role of type I collagen, the most abundant ECM component in the injured liver and a main contributor to tissue stiffness (28, 38). To test the role of CAF-derived type I collagen in metastatic growth, we crossed LratCre-transgenic mice with Col1a1$^{fl/fl}$ mice (Col1a1$^{\Delta HSC}$). Col1a1$^{\Delta HSC}$ mice displayed a strong reduction of *Col1a1* mRNA and fibrillar collagen deposition but no change in mRNA levels of other collagens or ECM-associated genes in comparison to their Col1a1$^{fl/fl}$ littermates (Figure 8B and Supplemental Figure 7B). Col1a1$^{\Delta HSC}$ mice also showed no change in immune-associated markers, apart from a modest decrease in *Cd4* and *Foxp3* mRNA levels (Supplemental Figure 7B). Unexpectedly, Col1a1 deletion significantly increased metastatic tumor growth, as evidenced by increased liver-to-body weight ratio and tumor area in both PDAC (Pan02, KPCY) and CRC metastasis (CMT93), which was paralleled by increased proliferation (Figure 8C, Figure 9A, and Supplemental Figure 7C). These findings were confirmed by a second approach, for which we crossed Mx1Cre mice with Col1a1$^{fl/fl}$ mice, an inducible model achieving deletion in all cells of the liver including HSC as well as a significant reduction of fibrillar collagen deposition (Supplemental Figure 7D). Similar to our data in Col1a1$^{\Delta HSC}$ mice, we observed a significantly increased tumor burden and proliferation in Mx1Cre-deleted mice (Supplemental Figure 7E). Consistent with the important role of type I collagen in tissue mechanics, tumors from Col1a1$^{\Delta HSC}$ mice displayed reduced expression of mechanosensitive transcriptional coactivators YAP and TAZ and stiffness (Figure 9B and Supplemental Figure 7F). These data were comparable with our finding that tumor cells plated on increasingly stiff plates in vitro upregulated tumor YAP/TAZ, indicating an increased mechanosensitive response to stiffness (Figure 9B). Based on these data, we hypothesized that type I collagen, despite activating mechanosensitive signals in tumor cells, could establish mechanical barriers that restrict tumor growth, overriding its tumor-promoting stiffness signals. To test this hypothesis, we developed a 3D in vitro culture model, in which we investigated how type I collagen could restrict tumor expansion as a mechanical barrier. When culturing cells in this 3D model in the presence of high collagen concentrations, we observed a significant reduction of tumor cell invasion as well as the number

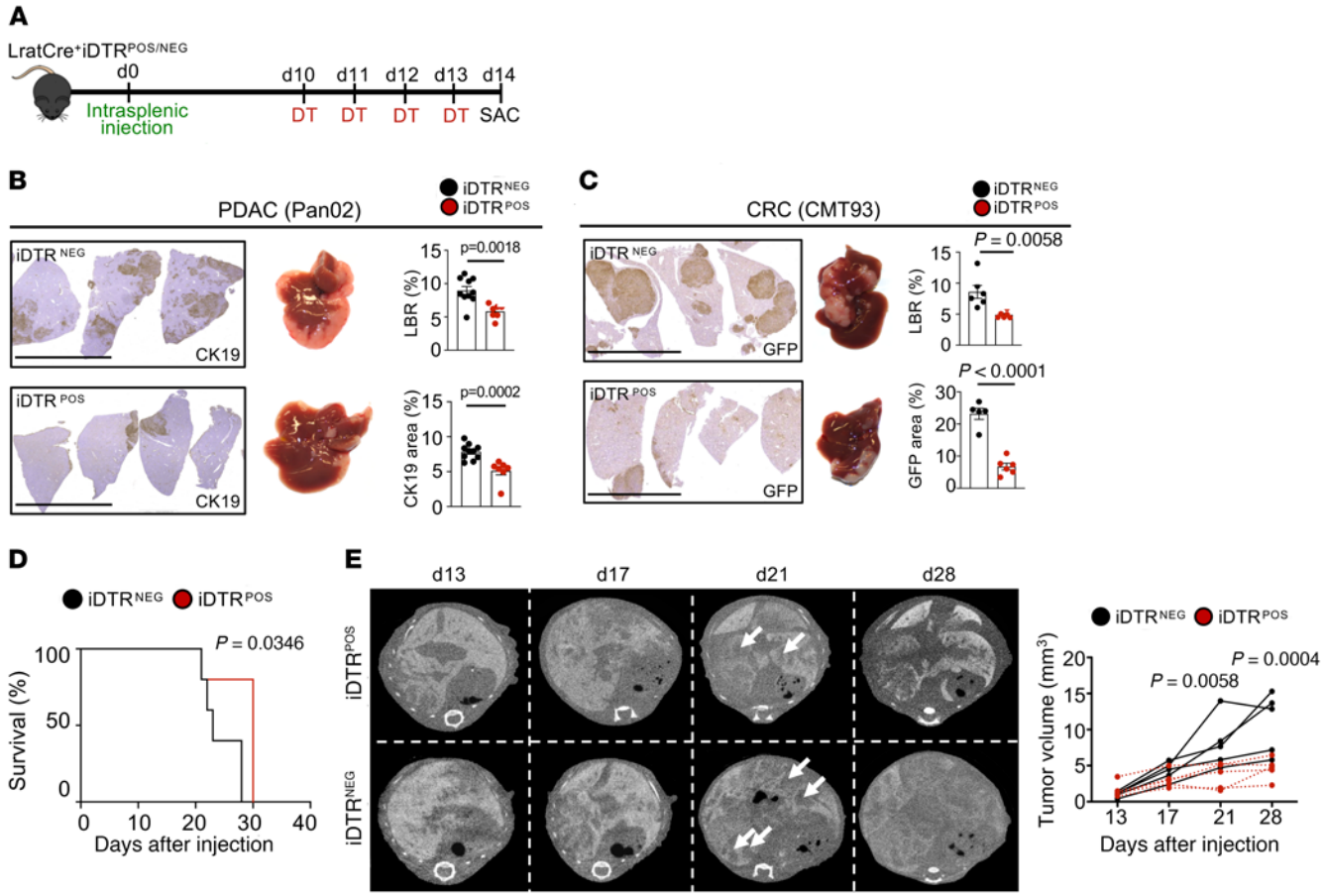

Figure 5. CAF depletion in advanced stages arrests growth and promotes survival. (**A**) HSC-CAF depletion via DT injection (0.5 ng/g) in LratCre$^+$TdTom$^+$ iDTR$^+$ or LratCre$^+$TdTom$^+$iDTR$^-$ littermates. (**B** and **C**) Representative macroscopic and IHC images of liver and liver-to-body weight ratio (LBR) and tumor area quantification (n = 6–8 mice/group), showing the effects of late HSC-CAF depletion on desmoplastic tumors (Pan02, CMT93). Scale bars: 1 cm. (**D**) Survival studies in iDTR mice injected with DT (n = 5 mice/group). DT was injected from day 13 onward at intervals of 3 days until the end of the study. (**E**) Contrast-CT scan analysis and tumor volume quantification of animals undergoing late HSC-CAF depletion via LratCre × iDTR. Arrows indicate metastatic tumors (dark areas); lighter areas show nontumor tissue. Statistics were done by 2-tailed unpaired t test or Mann Whitney U dependent on data distribution (**B**, **C**, and **E**) or Mantel-Cox test (**D**). Data are shown as the mean ± SEM.

of tumor colonies (Figure 9C), supporting our hypothesis that collagen physically restricts tumor spread. Given that deletion of CAF-derived type I collagen promoted metastatic tumor growth but that CAF depletion inhibited tumor growth, we next sought to identify CAF mediators responsible for increasing tumor growth.

myCAF-expressed Has2/HA promotes PDAC and CRC metastatic tumor growth. To test the hypothesis that myCAF promote metastatic tumor growth through noncollagenous ECM, we focused on *Has2*, encoding HA synthase 2, which is responsible for the majority of HA production in HSC and other cells (39), as one of the most upregulated genes in our bulk and scRNA-Seq CAF data (Supplemental Figure 8A). Moreover, high *HAS2*/HA expression has been linked to poor survival in primary CRC and PDAC (40, 41). *Has2* was highly expressed in the myCAF but not found in the iCAF or mesCAF clusters (Figure 10A). Consistent with our sequencing data, HA was abundant in desmoplastic liver tissue of mouse PDAC and CRC metastasis but negligible in nondesmoplastic models (Supplemental Figure 8B). Further, HA colocalized exclusively with tdTomato$^+$ CAF and not with GFP$^+$ or CK19$^+$ tumor cells (Supplemental Figure 8C). Consistent with our data showing high expression of *Has2* in HSC-CAF, we observed a drastic reduction of HA in our initial CAF depletion experiments (Supplemental Figure 8D). To functionally explore the role of HA, we next crossed LratCre with Has2$^{fl/fl}$ mice (Has2$^{\Delta HSC}$ mice), which reduced *Has2* mRNA and HA protein levels by >97% while leaving *Col1a1* and fibrillar collagen levels unchanged (Figure 10B and Supplemental Figure 8, E and F). To confirm that HA was present in human metastasis and thus a relevant target, we analyzed a cohort of 100 human CRC liver metastasis where 100% of patients had HA$^+$ staining but to varying degrees. In representative paired tumor and nontumor areas, we found a 10%–30% prevalence of HA within tumor areas, whereas nontumor areas contained significantly lesser HA (Figure 10C). Has2$^{\Delta HSC}$ mice displayed a strong reduction of tumor burden in terms of liver-to-body weight ratio as well as stained tumor area compared with their floxed littermates in our PDAC and CRC metastasis models (Figure 10D and Supplemental Figure 8G). In concordance with our observations in CAF-depleted mice, tumors had significantly reduced Ki67$^+$ proliferating cells (Figure 11A). Next, as HA has been described to have effects on tumor development not only via tumor cells but

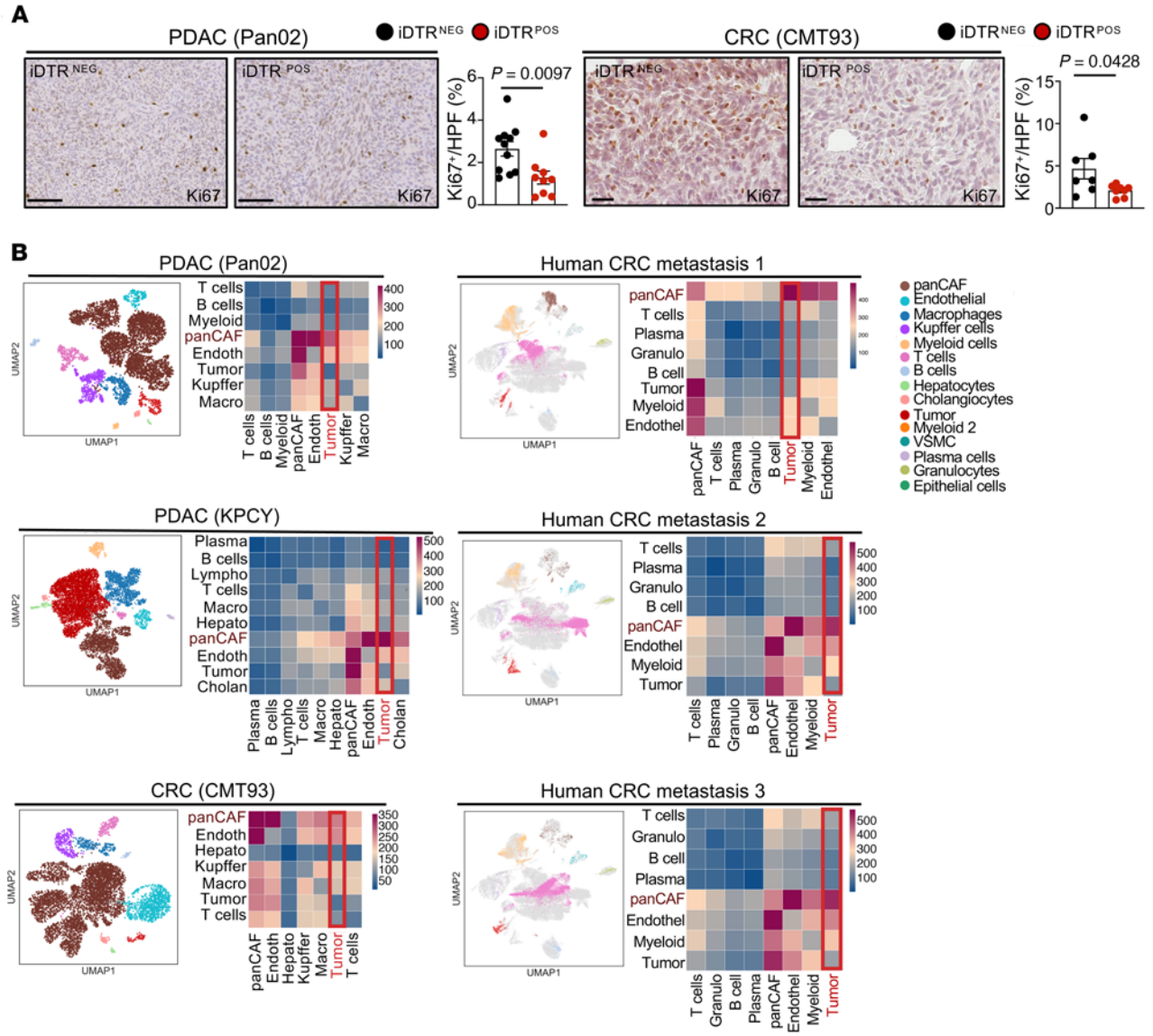

Figure 6. CAF promote tumor cell proliferation through direct interaction. (**A**) Representative IHC images and quantification of Ki67$^+$ cells in Pan02 and CMT93 models in iDTR models of CAF depletion. Scale bars: 1 cm. (**B**) UMAPs of scRNA-Seq displaying all cell populations in Pan02, CMT93, and KPCY models and human CRC liver metastasis, with accompanying CellphoneDB analysis showing ligand-receptor interactions between different cell populations. CellphoneDB analysis was performed on 3 CRC liver metastasis samples of 6 merged samples based on sufficient cell numbers for both CAF and tumor cells. Statistics were performed using 2-tailed unpaired *t* test or Mann Whitney *U* test dependent on data distribution (**A**). Data are shown as the mean ± SEM.

also other cell types, including immune cells, most prominently via T cells and T cell–expressed CD44 (42), we sought to establish if direct CAF-tumor interactions are sufficient to mediate tumor-promoting effects in the absence of adaptive immunity. To this end, we depleted CD4$^+$ and CD8$^+$ T cells from Has2$^{\Delta HSC}$ mice, which did not abolish the significant reduction of tumor burden in HA depleted animals, suggesting that tumor-promoting effects of HA were independent of T cells (Supplemental Figure 8H). We next explored how HA as a part of the matrix could influence tumor growth and invasive capacity, potentially exerting effects opposite to the restriction by type I collagen we had observed. As previous studies have shown that HA bioactivity is dependent on its size (43), we incubated tumor cells in the above-described 3D invasion model in the presence or absence of high-molecular-weight HA. 3D culture in the presence of HA promoted tumor invasiveness and resulted in higher numbers of invading subcolonies within the matrix compared with the Matrigel alone as well as Matrigel in combination with type 1 collagen (Figure 11, B and C). Moreover, coinjections of tumor cells and Has2 $^{\Delta HSC}$ HSC into *RAG2*$^{-/-}$ animals demonstrated strong reduction of tumor growth compared with tumors coinjected with Has2$^{fl/fl}$ control HSC, demonstrating immune-independent tumor promotion by HSC-produced HA (Figure 11D). Consistent with above data and our hypothesis that HSC-produced HA could directly act on tumor cells, we observed significant decreases in the size of spheroids, as well as reduced Ki67$^+$ expression in tumor cells, when we cocul-

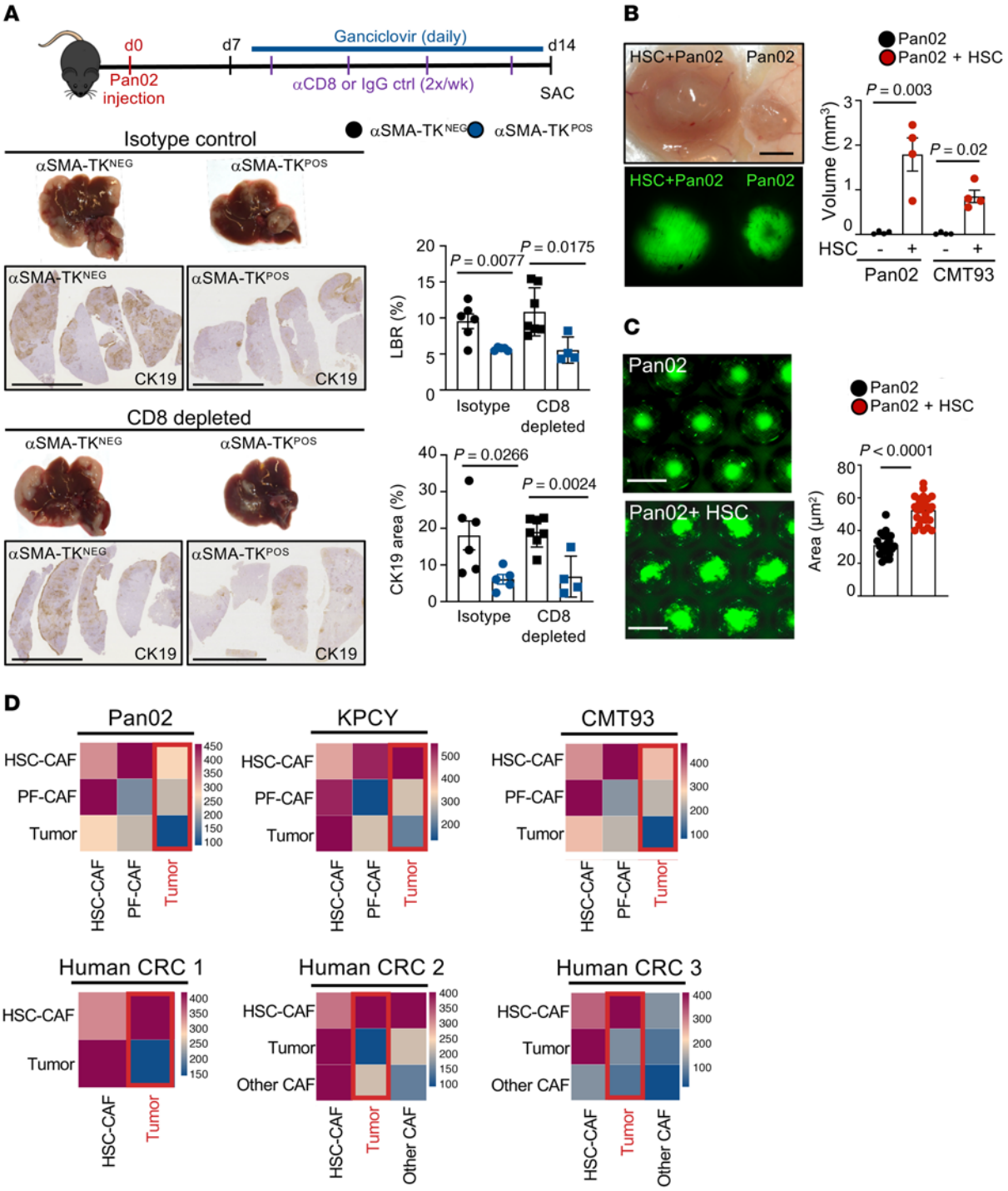

Figure 7. CAF promote tumor growth through direct interaction. (**A**) CD8⁺ T cell depletion or isotype injection in αSMA-TK mice injected with ganciclovir (i.p. 10 mg/kg) to deplete CAF simultaneously. Pan02 liver metastasis in αSMA-TK mice with representative macroscopic and IHC images of liver and liver-to-body weight ratio (LBR) and tumor area quantification (n = 5–7 mice/group). Scale bars: 1 cm. (**B**) Subcutaneous coinjection of HSC with tumor cells (Pan02 or CMT93) or tumor cells alone in immune-deficient *Rag2*$^{-/-}$ mice. (**C**) Representative pictures and quantification of cocultured spheroids comprising Pan02 cells alone and Pan02 cells with HSC. (**D**) CellphoneDB analysis showing ligand-receptor interactions between tumor cells with HSC-CAF and PF-CAF and/or other CAF in mouse and human liver metastasis samples. Statistics were performed using 2-tailed unpaired t test or Mann Whitney U test dependent on data distribution (**A–C**). Data are shown as the mean ± SEM.

tured tumor cells with HSC from Has2 $^{\Delta HSC}$ mice compared with coculture with Has2$^{fl/fl}$ HSC in spheroids or 2D models (Figure 11, E and F). Collectively, our results demonstrate direct tumor-promoting interactions between HSC-CAF and tumor cells, mediated by myCAF-derived HA, independent of adaptive immunity. Importantly, the tumor-, proliferation-, and invasion-promoting effects of myCAF-derived HA contrast the tumor-restricting role of myCAF-derived collagen.

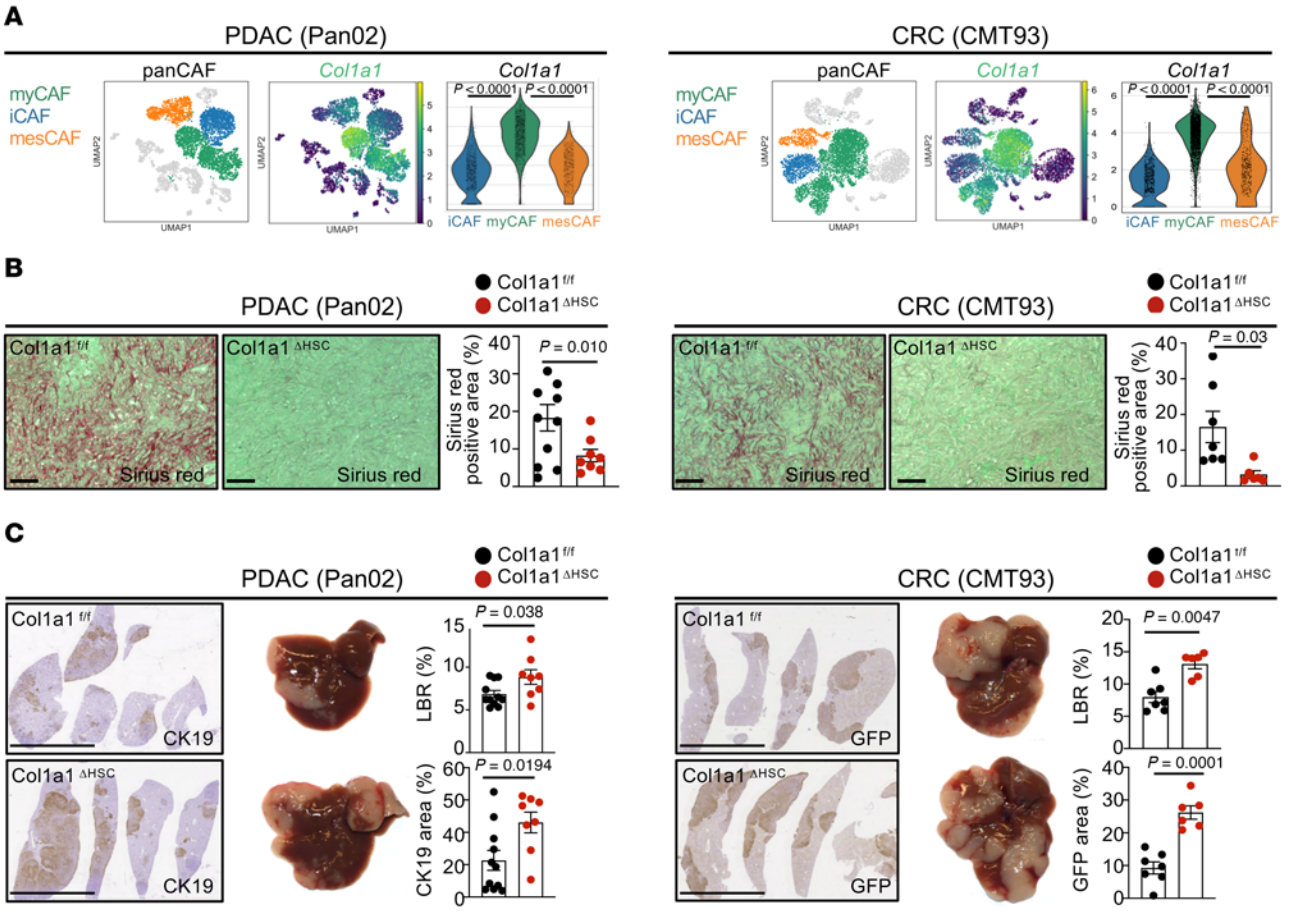

Figure 8. Type 1 collagen restricts tumor growth in vivo. (**A**) UMAPs and gene signatures of myCAF and *Col1a1* in Pan02 and CMT93 (n = 2). (**B** and **C**) Col1a1$^{f/f}$ and Col1a1$^{\Delta HSC}$ (n = 6–11 mice per group) were intrasplenically injected with Pan02 or CMT93 cells. (**B**) Sirius red staining. Scale bars: 100 μm. (**C**) Representative macroscopic and IHC images of liver and liver-to-body weight ratio (LBR) and tumor area quantification. Scale bars: 1 cm. Statistics were done using 2-tailed unpaired t test or Mann Whitney U test dependent on data distribution. Data are shown as the mean ± SEM.

iCAF mediator Hgf promotes PDAC and CRC metastatic tumor growth. Next, we sought to understand the role of iCAF, which was enriched for growth factors and chemokine signatures and displayed the strongest interactions with tumor cells in CellPhoneDB (Supplemental Figure 9A), suggesting tumor-promoting effects of this CAF population. Among the top-expressed iCAF genes was *Hgf* (Figure 12A), which, together with its receptor *Met*, expressed on tumor cells formed a ligand-receptor pair linking iCAF to tumor cells in our CellPhoneDB analysis (Supplemental Figure 9B). To determine the role of CAF-derived HGF, we crossed LratCre with Hgf$^{fl/fl}$ mice (Hgf$^{\Delta HSC}$), achieving a 70%–90% reduction of *Hgf* in PDAC and CRC liver metastases while leaving HSC marker *Lrat* as well as ECM-modulating myCAF gene *Col1a1* intact (Supplemental Figure 9C). In these models, Hgf$^{\Delta HSC}$ mice displayed a significantly reduced tumor burden in all desmoplastic models, as shown by reduced liver-to-body weight ratio and tumor area (Figure 12B and Supplemental Figure 9D), which was accompanied by a reduction in Ki67$^+$ proliferating tumor cells (Figure 13A and Supplemental Figure 9D). In vitro, HGF treatment increased tumor cell proliferation and, as determined by phospho-kinase screen and immunoblotting, increased Erk phosphorylation (Figure 13B). Further, when cells were pretreated with Met inhibitor Merestinib or Erk inhibitor U0126 proliferation was significantly reduced (Figure 13C). Together, our in vitro and in vivo findings demonstrate that iCAF directly interacts with tumor cells via the HGF-MET ligand-receptor pair, promoting tumor cell proliferation and desmoplastic tumor growth in the liver, suggesting that iCAF and myCAF may synergistically enhance tumor growth through distinct mediators.

Discussion

CAF may exert tumor-promoting and tumor-restricting functions (12–18), but the mechanisms that underlie these opposing actions remain only poorly understood. Much of the literature on CAF has closely linked the entities CAF, ECM, desmoplasia, and stiffness, suggesting that, in desmoplastic tumors, a dominant biological effect of CAF is production of type I collagen and/or other ECM, leading to increased stiffness and activation of mechanosensitive signaling (27–29). Our studies in mice with CAF-selective deletion of type I collagen challenge above paradigm on the type I collagen–stiffness pathway as dominant force in the tumor microenvironment, suggesting that the mechanical restriction by type I collagen overrides its stiffness-mediated tumor-promoting actions. Moreover, our data demonstrate that the over-

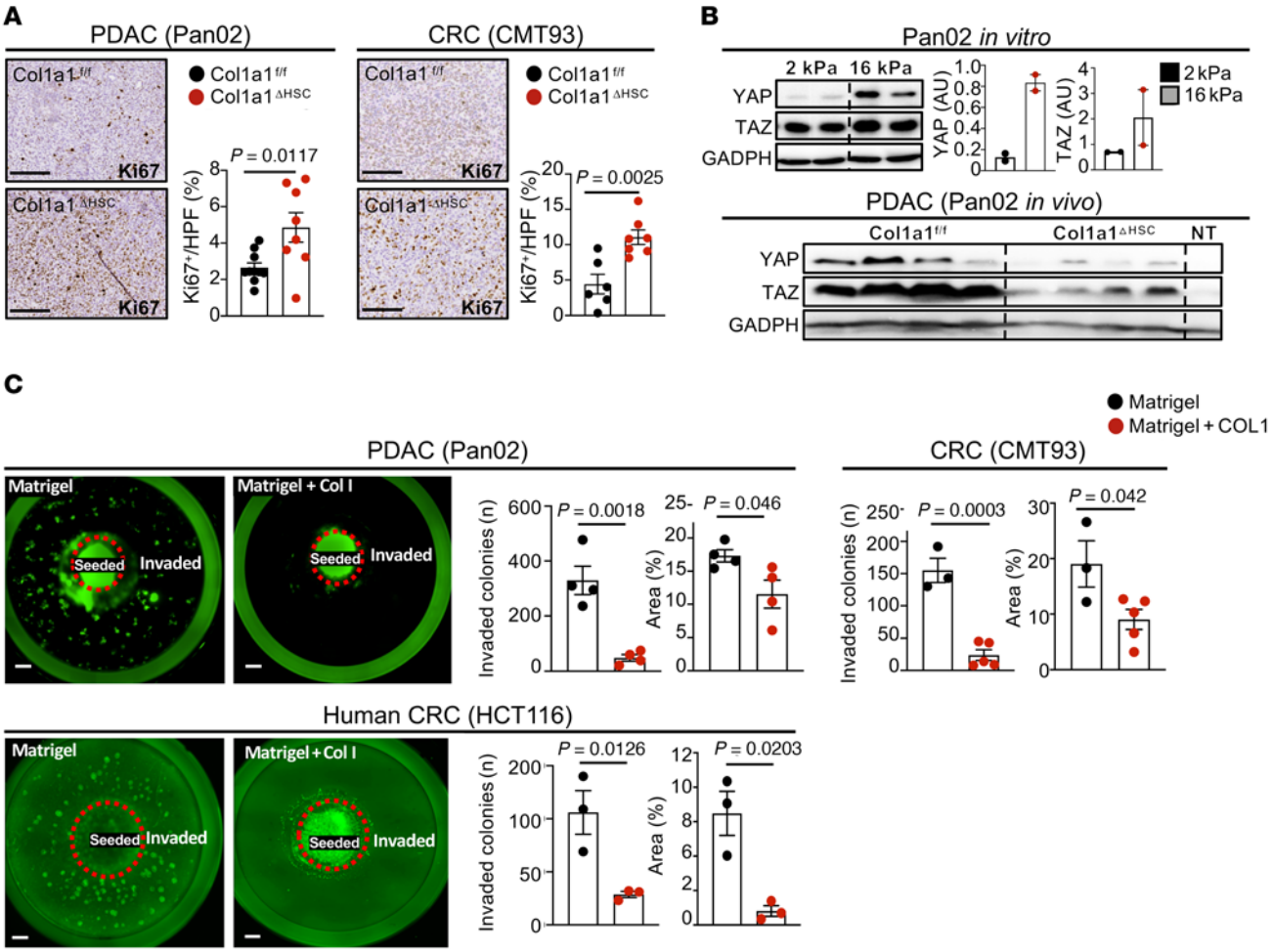

Figure 9. Type 1 collagen restricts tumor growth independent of stiffness. (**A**) Col1a1$^{fl/fl}$ and Col1a1$^{\Delta HSC}$ (n = 6–11 mice per group) were intrasplenically injected with Pan02 or CMT93 cells. Representative images and quantification of Ki67$^+$ cells. Scale bars: 100 μm. (**B**) YAP and TAZ Western blot and quantification in cells plated on soft (2 kPa) or stiff (16 kPa) plates and Western blot from Col1a1$^{fl/fl}$ and Col1a1$^{\Delta HSC}$ nontumor and tumor tissue (nontumor, NT, n = 1; tumor n = 4 mice per group) in the Pan02 liver metastasis model. (**C**) Representative images and quantification of an in vitro collagen-Matrigel assay, with cells seeded in the center and invading cells in the periphery in Matrigel alone or Matrigel and type 1 collagen (5 mg/ml) day 10 or day 12 (HCT116) after seeding (n = 3–4 wells per group). Statistics were done using 2-tailed unpaired t test or Mann Whitney U test dependent on data distribution (**A–C**). Data are shown as the mean ± SEM.

all tumor-promoting effects of CAF, evidenced by two different genetic depletion strategies, are mediated by other CAF-secreted factors that dominate over the tumor-restricting effects of collagen. Rather than targeting the entire CAF population, which would inhibit the tumor-restricting effects of type I collagen, one could instead selectively target tumor-promoting CAF mediators such as HGF and HA. Of note, while both *Has2* and *Col1a1* were expressed by myCAF, suggesting that myCAF are capable of switching from tumor suppressing to tumor promoting, the majority of high collagen expressors were *Has2*^{lo} (Supplemental Figure 10). This may either be due to a different trajectory the cells take and/or due to the high bioenergetic requirements for the production of these ECM mediators, making it difficult to produce large amounts of type I collagen and HA at the same time.

A second key finding of our study is that direct interactions between HSC-derived CAF and tumor cells represent a main mechanism of tumor promotion and restriction in desmoplastic liver metastasis. We could show this using 3 different cell lines, including intrasplenically injected KPCY cells that are histologically identical to the natural liver metastasis observed in *KrasLSL.*$^{G12D/+}$; *p53*$^{R172H/+}$; *PdxCre*$^{tg/+}$ (KPC) animals, a well-validated PDAC model, thus underscoring the relevance of our results (Supplemental Figure 11). Consistent with our CellPhoneDB analysis, which found HSC-CAF and tumors to have the strongest interactions, we observed direct tumor-promoting effects of HSC in cocultures and coinjection experiments. Accordingly, we also found direct effects of type I collagen, HA and HGF on tumor cells in 3D culture, coculture and coinjection studies. With a strong focus on the field on CAF-immune cell interactions in recent years, we still observed strong tumor-promoting effects of CAF in coinjection studies in *RAG2*$^{-/-}$ mice, which lack adaptive immunity, as well as in mice with depletion of CD4$^+$ and CD8$^+$ cells. At the same time, we do not exclude that CAF may exert effects on metastatic growth in the liver by regulating antitumor immunity in addition to above-discussed direct interactions. In this regard, while we found only minor effects of CAF depletion on the composition of

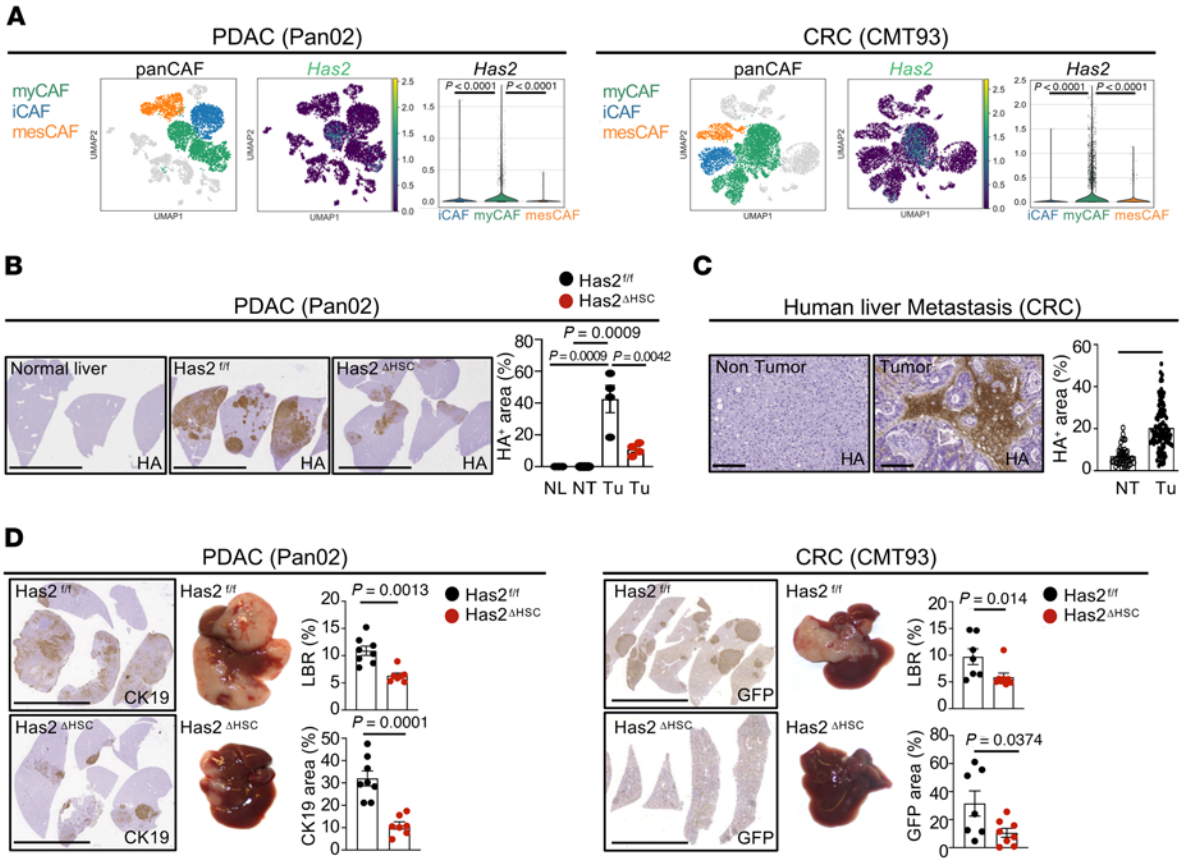

Figure 10. myCAF-enriched HA promotes tumor growth in vivo. (**A**) UMAPs and gene signatures of myCAF and *Has2* in Pan02 and CMT93 (n = 1 each). (**B**) Efficient reduction of HA shown by IHC in Has2$^{\Delta HSC}$ mice compared with Has2$^{fl/fl}$ littermates (NL, normal liver; NT, nontumor; Tu, tumor). (**C**) Representative IHC and quantification of HA staining in human CRC liver metastasis with matched nontumor tissue (n = 100). Scale bars: 100 μm. Statistics were done using Paired t test. (**D**) Representative macroscopic and IHC images of liver and liver-to-body weight ratio (LBR) and tumor area quantifications (n = 7–8 per group each). Scale bars: 1 cm. Statistics were done using 2-tailed unpaired t test or Mann Whitney U test dependent on data distribution (**B** and **D**) and Wilcoxon's matched-pairs signed-rank test (**C**). Data are shown as the mean ± SEM.

immune cells in the liver, we did observe a significant decrease of Foxp3$^+$ Tregs. Likewise, our analysis of tumors in mice with Col1a1 deletion did not reveal major differences in immune and inflammatory markers. However, we cannot exclude that the intrasplenic tumor model is too brief to fully reveal the effects of antitumor immunity. Alternatively, effects of CAF on immunity may be less relevant in the liver than in other organs due to its immune-privileged nature (44, 45), rendering additional immunomodulation by CAF and CAF-secreted mediators ineffective, which would also explain the lacking effects in our CD8$^+$ cell depletion experiments.

Finally, our study revealed HSC as main source of CAF in murine and human liver metastasis by genetic tracing and scRNA-Seq analysis. Accordingly, mesCAF, expressing a population that is analogous to PFs in liver fibrosis, only constituted a minor contributor to the CAF pool. The strong effects of HSC-CAF depletion and HSC-CAF–specific knockout of HGF and HAS2 on tumor size and survival suggest that HSC-CAF and their mediators may represent a therapeutic target for the treatment of desmoplastic liver metastasis. Knowledge about these specific tumor-promoting and tumor-restricting mediators could be therapeutically exploited for tailored therapies, allowing for inhibition of tumor-promoting mediators while sparing or even additionally boosting tumor-restrictive pathways. In view of the disappointing results of HA-degrading PEGPH20 in pancreatic cancer (46), possibly due to proinflammatory effects of the degraded low-molecular-weight HA (43), other inhibitors of HA-induced signals or inhibitors of HGF/MET signaling may be considered. In this context, future studies should investigate whether CAF depletion or long-term inhibition of tumor-promoting CAF mediators promote survival in preclinical studies or if they could make tumors more aggressive, as observed for other forms of tumor therapy (17, 18, 47).

Methods

Human specimens. Samples from patients with CRC liver metastases (LM) were analyzed. All patients underwent planned curative surgery at the Department for General, Visceral and Transplantation Surgery, University Hospital Heidelberg. Tissue samples of 100 patients with LM were used for IHC. All patient data was deidentified.

Animal models. Animal experiments were performed on 8- to 12-week-old female or male mice maintained in a specific pathogen–free environment and fed with a standard diet. C57BL/6J, TdTomato Ai14 reporter (TdTom), Rosa26-iDTR (iDTR), Mx1-Cre, and *RAG2*$^{-/-}$ animals were purchased from The Jackson Laboratory. Col1a1-GFP reporter mice and Lrat-Cre mice (26) have been described before and

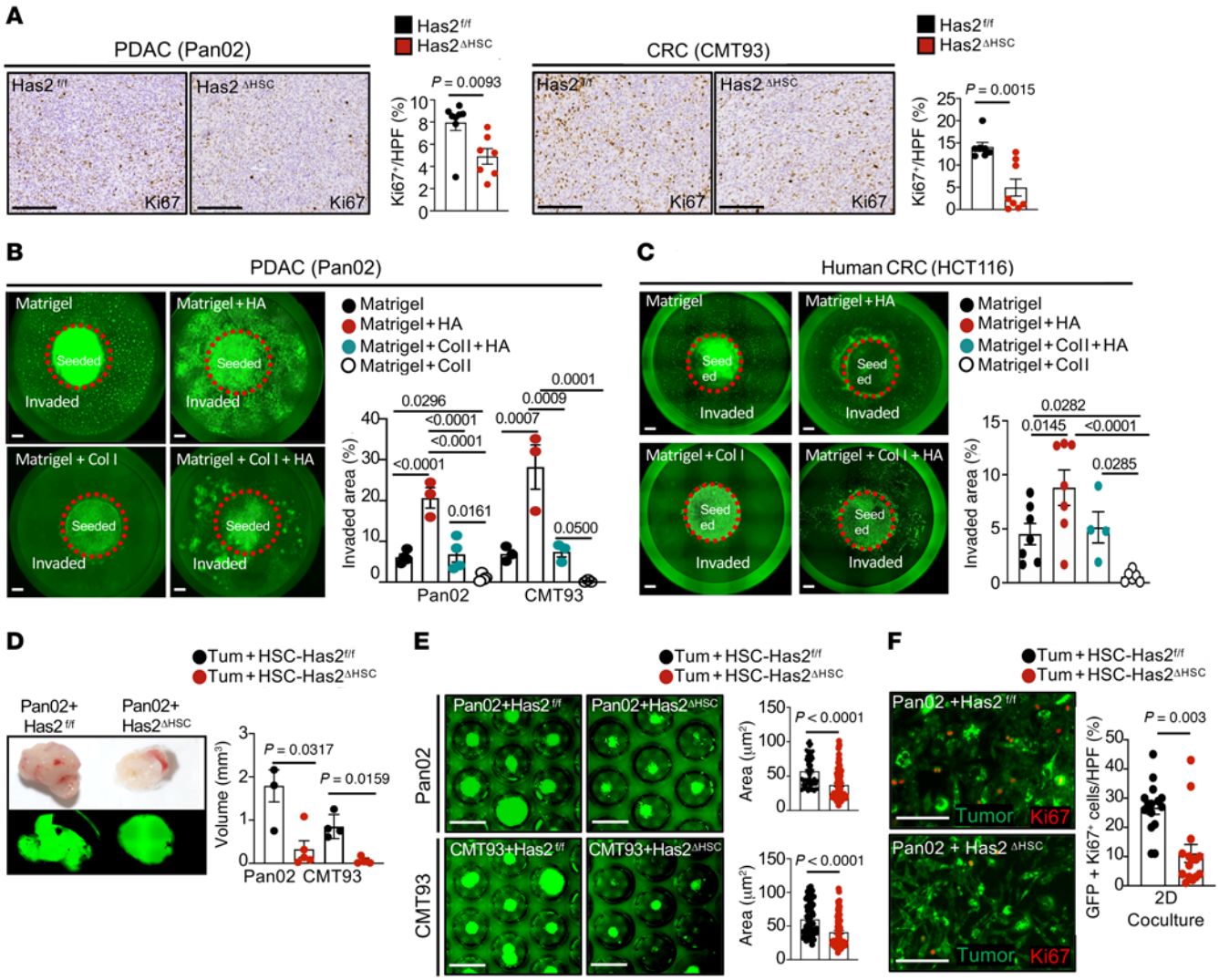

Figure 11. HA promotes tumor cell growth and invasiveness. (**A**) Representative IHC images and quantification of Ki67⁺ cells in Pan02 and CMT93 models in Has2$^{fl/fl}$ and Has2$^{\Delta HSC}$ animals (n = 7–8 per group). Scale bars: 100 μm. (**B** and **C**) Representative images and quantification of in vitro Matrigel assay, with cells seeded in the center and invading cells in the periphery in Matrigel alone, Matrigel and high-molecular-weight HA, Matrigel and HA and type 1 collagen, or Matrigel and type 1 collagen (HA and type I collagen: 2.5 mg/ml) day 6 after seeding (n = 3–4 per group each). (**D**) Coinjection of Has2$^{fl/fl}$ and Has2$^{\Delta HSC}$ with tumor cells (Pan02 or CMT93) in *RAG2*$^{-/-}$ mice. (**E** and **F**) Representative images and quantification of cocultured spheroids (**D**) or 2D cocultures (**E**) and Ki67⁺ cells comprising Has2$^{fl/fl}$ and Has2$^{\Delta HSC}$ with Pan02 tumor cells. Statistics were done using 2-tailed unpaired t test or Mann Whitney U test dependent on data distribution (**A** and **D**–**F**) or 1-way ANOVA using Fisher's LSD test (**B** and **C**). Data are shown as the mean ± SEM.

were backcrossed 5 times to C57BL/6. αSMA-TK mice were provided in-house. For HSC-selective deletion of *Col1a1*, *Hgf*, and *Has2*, Lrat-Cre mice were crossed with Col1a1 mice (48) and Hgf- (49) and Has2-floxed (39) animals.

Cell lines and cell culture. Murine Panc02 (designated Pan02 according to common name; NIH repository), CMT93 (ATCC), B16F10 (ATCC), and EO771 (CH3 Biosystems) cells stably expressing GFP were established by transfection with lentiviral vector (Addgene) carrying a puromycin resistance gene. The primary pancreatic tumor cell line derived from the spontaneous KPCY model of PDAC was provided in-house, as was the human cell line HCT116. Pan02 and EO771 cells were cultured in RMPI 1640 (Gibco). CMT93, B16F10, KPCY, and Panc1 cells were cultivated in DMEM (high glucose, Gibco). HCT116 cells were cultured in MyCoy's 5A media (Gibco). All media were supplemented with 10% FBS (Gibco), 1% antibiotic-antimycotic (Gibco), 1–4 μg/mL puromycin (Thermo Fisher Scientific) at 37°C and 5% CO_2 in a humidified atmosphere. The concentration of puromycin used (for lentiviral-GFP transfected cells) was predetermined through resistance of initially transfected cells. For some experiments, cells were treated with recombinant mouse HGF (R&D Systems), Erk inhibitor U0126 (Cayman Chemical), or MET inhibitor merestinib (Selleckchem).

Liver metastasis model. Surgical procedures were as described previously (50), with some modifications. Briefly, subconfluent cells were harvested, washed, and resuspended in PBS just before intrasplenic injection. Mice were anesthetized and an incision was made to exteriorize the spleen, which was further divided using 2 horizon clips (Telefax). The upper lobe was separated and placed back into the body cavity, and the distal section of the spleen was inoculated with 10^6 Pan02 cells, 0.7×10^5 CMT93 cells, 0.5×10^5 KPCY cells, 0.1×10^5

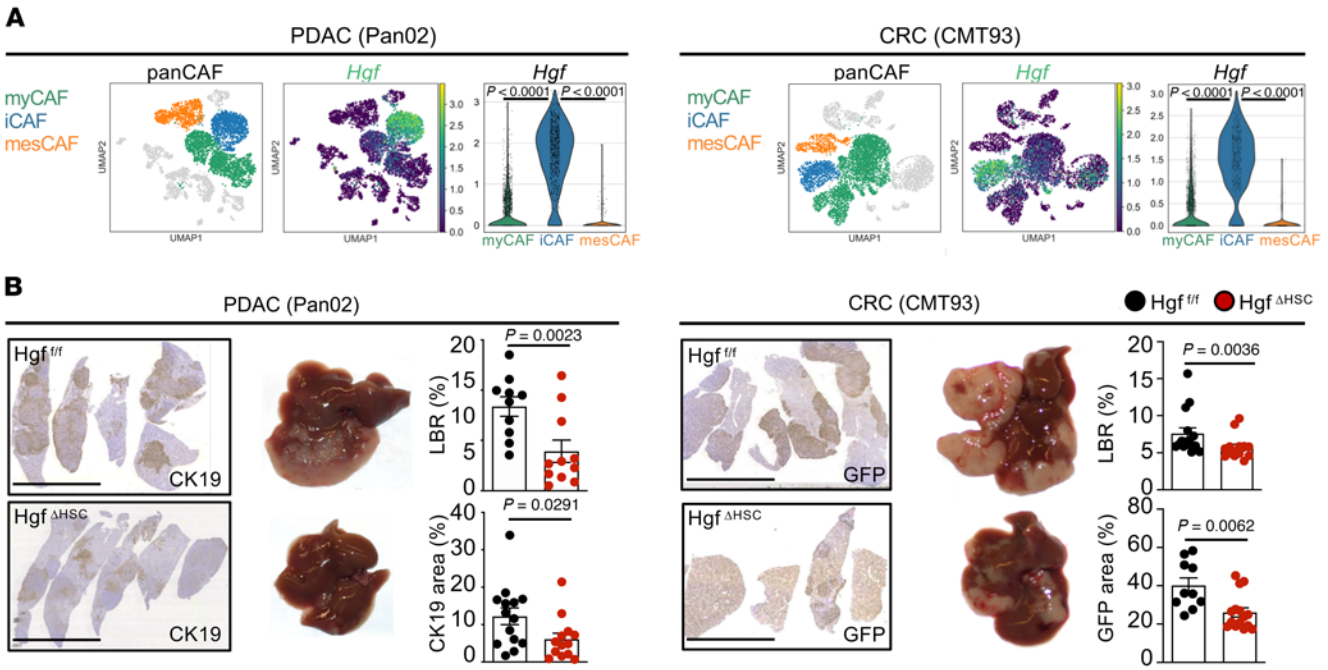

Figure 12. iCAF-enriched Hgf promotes tumor growth in vivo. (**A**) UMAPs and gene signatures of iCAF and *Hgf* in Pan02 and CMT93 (n = 2). (**B**) Representative macroscopic and IHC images of liver and liver-to-body weight ratio (LBR) and tumor area quantification (n = 10–15 per group each). Scale bars: 1 cm. Statistics were done using 2-tailed unpaired t test or Mann Whitney U test dependent on data distribution. Data are shown as the mean ± SEM.

B16F10 cells, or 0.25 × 10^5 EO771 cells in 100 μL PBS. The syringe needle was kept in place for 90 seconds, followed by a cotton swab to stymie any bleeding for 45 seconds, followed by sutures below the hemispleen. The hemispleen containing inoculated cells was then resected to prevent growth of primary tumor. The abdominal wall was closed with 4–0 polyglycolic acid sutures (Henry Scientific) and 7 mm wound clips (Braintree Scientific) were used to close the skin incision. Animals were monitored every day until day 14 or day 16, when they were euthanized, and the liver was harvested and processed.

In vivo cell depletion. In order to deplete HSC-CAF, Lrat-Cre$^+$iDTR$^+$ TdTom$^+$ or LratCre$^+$iDTR- TdTom$^+$ littermates were intraperitoneally injected with DT (MilliporeSigma, 0.5 ng/g body weight) at intervals indicated in figures. For genetic depletion of CAF, αSMA-TK$^+$ mice or their αSMA-TK$^-$ littermates were injected intraperitoneally with ganciclovir (Invitrogen) at a concentration of 10 mg/kg at intervals indicated in figures. *Col1a1* deletion in Mx1-Cre Col1a1 animals was carried out by injecting poly I:C (MilliporeSigma) 3 times 2 days apart when animals were 5 weeks old. This was followed by a rest period of 4 weeks till animals were surgically manipulated. CD8 and/or CD4 depletion was carried out twice a week at 200 μg/mouse/day using anti-CD8 and/or anti-CD4 InvivomAb antibody (BioXCell) intravenously.

In vivo imaging. Mouse livers were imaged using the Quantum FX microCT imaging system of the HICCC OPTIC core. ExiTron nano 6000 CT contrast agent for preclinical imaging (Miltenyi Biotech) was used, and microCT was performed 4 times after injection of tumor cells, starting 10 days after injection. Respiratory gating was utilized to allow for high resolution of the body without blurring of the objects of interest. A single scan of 34 seconds was taken, and the animal was then removed from the micro-CT and returned to its cage and kept warm to keep homeothermic stability until consciousness returned.

IHC, immunofluorescence, and quantification. Paraffin-embedded or frozen liver sections were incubated with the primary antibodies: CK19 (1:500, Abcam), GFP (1:300, Abcam), Ki67 (1:100, Abcam), cleaved caspase-3 (1:200, Cell Signaling), and αSMA (1:200, MilliporeSigma). Recombinant HABP protein (rhAggrecan aa30-675/His [NSO/7], biotinylated, R&D Systems), at 4 μg/ml, was used as described previously (39) to detect hyaluronin in liver tissue sections. The Vectastain Elite ABC-HRP kit (Vector Laboratories) and the DAB Peroxidase Substrate kit (Vector Laboratories) were used to detect conjugates, followed by counterstaining with hematoxylin. Alternatively, fluorescent secondary antibodies with different fluorescent conjugates (donkey anti-rabbit Alexa Fluor 488, 1:500, Life Technologies; donkey anti-mouse Alexa Fluor 488, 1:500, Life Technologies) with streptavidin signal amplification (Alexa Fluor 594/647, 1:500, Life Technologies) were employed followed by DAPI (Thermo Fisher Scientific). Nonfluorescent image acquisition was done with a Leica SCN400 slide scanner or Olympus IX71S1F-3 microscope coupled to a QImaging Retiga camera. Quantification of DAB area was performed using the LEICA Digital Image Hub 4.0 image server. All IHC- and immunofluorescence-based quantification was performed on sections containing representative tissue from several lobes of the liver (3–5 midsized tissue pieces per liver per mouse). For tumor area quantification (CK19 or GFP), the entire slide was quantified semiautomatically at ×4, whereas for Ki67 and cleaved caspase-3 staining, 5 fields/section within tumor areas were quantified at ×10. Fluorescence images were captured at ×2, ×10, ×20, or ×40 magnification employing a Olympus IX71S1F-3 microscope, Keyence fluorescence microscope (BZ-X800), or Nikon A1 confocal laser microscope (Nikon Instruments). Images were analyzed using Fiji and Adobe Photoshop.

Sirius red staining and quantification. Picrosirius red staining was done on paraffin liver sections. Images were taken in 5 fields with ×10

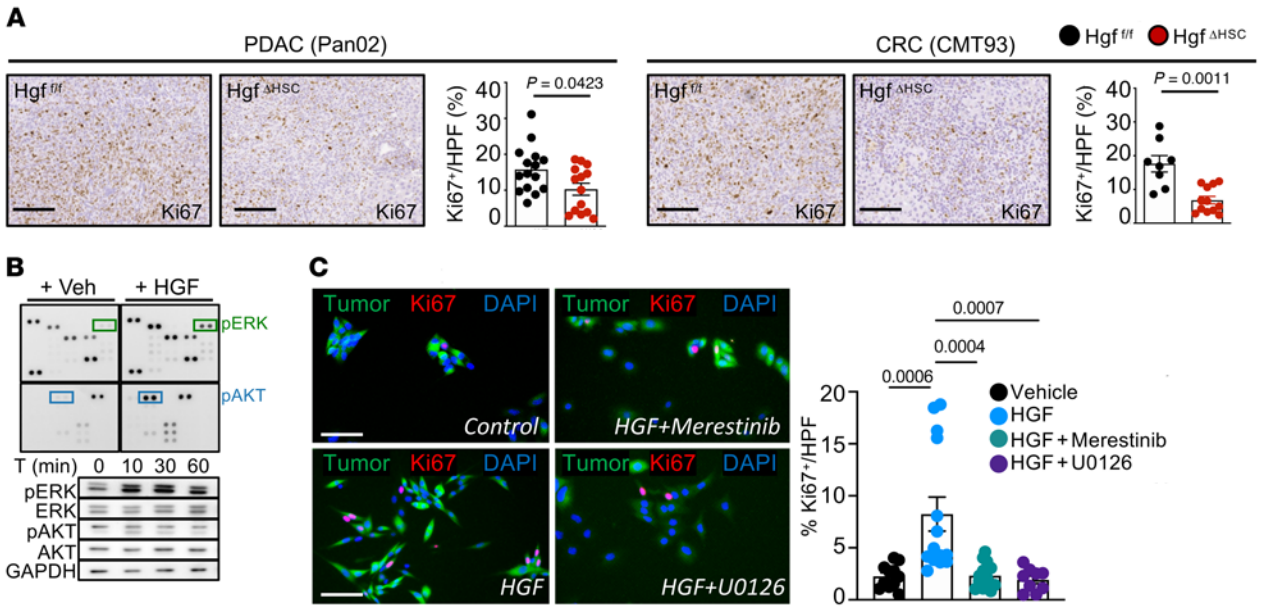

Figure 13. Hgf promotes tumor cell proliferation through Met receptor. (**A**) Representative IHC images and quantification of Ki67$^+$ cells in Pan02 and CMT93 models in Hgf$^{fl/fl}$ and Hgf$^{\Delta HSC}$ animals (n = 10–15 per group). Scale bars: 100 μm. (**B**) Pan02 cells treated with recombinant mouse HGF (25 ng/ml) or vehicle for 10 minutes followed by a phospho-kinase array and Western blot for phosphorylated and total ERK1/2 and AKT. (**C**) Pan02 cells treated with HGF (25 ng/ml) or Merestinib (3 mM) or U0126 (10 mM) and followed by recombinant mouse HGF (25 ng/ml) or vehicle for 48 hours followed by Ki67 staining. Scale bars: 250 μm. Statistics were done using Mann Whitney U test or unpaired t test dependent on data distribution (**A**) or 1-way ANOVA with Kruskal Wallis post hoc test (**C**). Data are shown as the mean ± SEM.

magnification per mouse using a polarized light filter. Quantification was performed using Adobe Photoshop software. For all IHC and Sirius red staining, similar sized tumors were quantified between genetically modified mice and their littermates.

Western blot and phosphokinase array. Cell or tissue extracts were processed using RIPA buffer with PhosSTOP phosphatase inhibitor (Roche) containing complete protease inhibitor (Roche). Proteins were separated with a 10% SDS-PAGE and blotted on a nitrocellulose membrane (MilliporeSigma) using a semi-dry blot system (Bio-Rad). The following primary antibodies were used: p-ERK1/2 (1:2000, Cell Signaling, 4370), ERK1/2 (1:1000, Cell Signaling, 4695), p-AKT (1:2000, Cell Signaling, 4060), AKT (1:1000 Cell Signaling, 9272), and YAP/TAZ (1:1000, Cell Signaling, 8418) followed by exposure to horseradish peroxidase–conjugated secondary antibody against rabbit IgG (1:5000, Santa Cruz, sc-2004). GAPDH (1:15,000, MilliporeSigma, G9295) was used to establish equal loading of proteins. Membranes were then incubated with SuperSignal West Femto Maximum Sensitivity Substrate (Thermo Fisher Scientific) and exposed, and bands were quantified with ImageJ software (NIH). When required, stripping was conducted with Restore Western Blot Stripping Buffer (Thermo Fisher Scientific).

Cell isolations and coculture and coinjection studies. Tumors were resected under aseptic conditions and mechanically dissociated using sterile scissors into 1 mm^3 pieces in 2 ml FBS-free DMEM high glucose medium (Gibco). 5 ml trypsin-EDTA (Gibco) was added and the solution was placed at 37°C with frequent inversions for 30 minutes. Subsequently, 1% DNase (Roche) and 2 ml DMEM with 10%FBS were added, and the solution was filtered through a 70 μm cell strainer. Separation was performed using flow cytometry to segregate GFP$^+$ tumor cells. These cells were subsequently used for in vivo passage and surgeries, RNA-Seq, or in vitro assays. HSC were isolated from animals as described previously (26). For CAF isolations, a similar protocol was followed with increased concentrations of pronase (0.4 mg/ml), collagenase D (1.3 mg/ml), and mixed solution (0.5 mg/ml pronase and 0.3 mg/ml Collagenase D), which were subsequently subjected to a 34% Nycodenz gradient. Purity was assessed with a flow cytometer (BD Aria). Cells were used for scRNA-Seq or bulk RNA-Seq or in vitro assays. 2D or 3D (spheroid) cocultures were performed on plastic plates or 96-well low-attachment plates (Corning) by coplating HSC and tumor cells in a 1:1 ratio. For subcutaneous coinjection studies, tumor cells were injected into the flanks of *RAG2*$^{-/-}$ mice in the absence or presence of HSC of a specific genotype as indicated, in either side of the same mouse. Mice were sacrificed 14 days afterward, and tumors were weighed; tumor size was measured with calipers, and volume was calculated. The collagen-Matrigel or collagen with high-molecular-weight hyaluronic acid assays were prepared as follows: 200 μl pipette tips were cut at the larger end, autoclaved, and placed at 4 degrees along with a 24-well plate. A tip was placed in the center of the well and Matrigel alone, Matrigel with a high concentration of collagen (10 mg/ml, Corning), or Matrigel with high-molecular-weight HA (R&D Systems) was poured on the outside of the tip (500 μl total volume). The total concentration of either collagen or HA was 5 mg/ml. All materials were precooled and immediately applied to ensure homogeneity. Plates were then placed at 37 degrees for 3 hours, followed by addition of warm PBS overnight. PBS was aspirated carefully the next morning, tips were removed with sterile forceps, and 30,000 cells (in 40 μl) were added to the center of the well. Cells were allowed to settle for 1 hour before prewarmed media were added. Media were replaced every 3 days, and images were acquired at day 6 and day 10 using a Keyence fluorescence microscope (BZ-X800).

Immune cell isolation and flow cytometry. Immune cell subsets were isolated from the tumors and quantitatively analyzed. After weighing

tumors and mechanical homogenization, tumors were digested (collagenase A, 1 mg/ml, Roche) and DNase I (0.5 μg/ml, Roche) in media (RPMI 1640 supplemented with 5% FBS, 1% L-glutamine, 1% penicillin-streptomycin, and 10 mM HEPES)) with 40 minutes of shaking (150 rpm at 37°C). The cells were then filtered through 100 μm sterile strainers and washed and staining was performed. The lymphoid subset underwent a separation gradient using Percoll (67%, 40%), followed by staining along with previously separated myeloid cells. Dead cells were excluded using Ghost Dye cell viability reagent. The following antibodies were used for extracellular staining: anti-CD45 (BD and Biolegend, 1:400), anti-B220 (BD, 1:200), anti-CD19 (Tonbo, 1:200), anti-CD4 (BD, 1:400), anti-CD8 (Tonbo, 1:400), anti-NK1.1 (BD, 1:300), anti-CD11b (BD, 1:500), anti-CD11c (BD, 1:200), anti-F4/80 (Tonbo, 1:500), and anti-MHC class II (Tonbo, 1:400) antibodies. Intracellular antibodies included the following: anti-CD3e (BD, 1:400), anti-TCRβ (BD, 1:300), and anti-Foxp3 (Thermo Fisher Scientific, 1:300). Cells were fixed and permeabilized using the FOXP3/transcription factor staining buffer set (Tonbo) according to the manufacturer's instructions. Samples were acquired using a BD LSRFortessa cell analyzer and analyzed using FlowJo (v10).

Data and material availability. Raw and metadata associated with RNA-Seq are available in the Gene Expression Omnibus (GEO) database (accession GSE160541).

Additional details on scRNA-Seq, CellPhoneDB analysis, bulk RNA-Seq, RNA isolation, quantitative real-time PCR, and rheometry are provided in the Supplemental Methods.

Statistics. Statistical analysis was performed using GraphPad Prism v.7.0 and v.8.0. D'Agostino and Pearson omnibus normality tests and Shapiro-Wilk normality test (in case sample size was too small for the former) were performed to assess the nature of the data sets. Parametrically distributed data were analyzed using the unpaired 2-tailed *t* test (2 groups), and Mann-Whitney *U* test was used for nonparametric data. For more than 2 groups, 1-way ANOVA was conducted; if significant, a multiple-comparison analysis was performed. For nonparametric data, a Kruskal-Wallis test with a confidence interval of 95% was employed with a Dunn multiple-comparison post hoc test. For Kaplan-Meier survival experiments, a log-rank (Mantel-Cox) test was employed. Results with a *P* value of less than 0.05 were considered as significant. As indicated in each figure legend, *n* represents the number of mice.

Study approval. Samples from patients with CRC LM were analyzed. The study was approved by the local ethics committee (ethics commission of the medical faculty of the Heidelberg University) (S-080/2013 and 323/2004). Informed consent was obtained from all patients.

All animal experiments were approved by the Institutional Animal Care and Use Committee of Columbia University (protocols AC-AAAO7402, AC-AAAY8467, and AC-AAAZ4481) and the Lower Saxony State Office for Consumer Protection and Food Safety, Germany (protocol 15-1848).

Author contributions

SB designed experiments; generated, analyzed, and interpreted data; and drafted the manuscript. FH performed data generation and analysis. AR performed data generation and analysis. M. Miller performed computational analysis, including bulk RNA-Seq and scRNA-Seq and CellPhoneDB analyses. SA generated mouse lines and performed experiments. AN performed computational analysis of human scRNA-Seq and CellPhoneDB analyses. AF generated mouse lines and generated data. LC performed stiffness experiments. TMS and NA assisted with flow cytometry analysis. AM performed quantifications. DY provided technical assistance. PAS assisted with analysis. BZS and KPO provided KPCY cell lines and KPC liver specimens, respectively. NMW and TS provided CRC metastasis human samples and assisted with analysis of data;.ES generated LratCre Has2$^{fl/fl}$ mice. M. Mack contributed Col1a1-floxed mice. DZ provided human single-cell data for CRC metastasis. RK provided αSMA-TK mice and scientific advice. RGW supervised stiffness experiments and analysis. IM conceived the study, designed experiments, and edited the manuscript. RFS conceived and oversaw the study, designed experiments, and edited the manuscript.

Acknowledgments

RFS was supported by NIH grants CA190844 and CA228483; IM was supported by a fellowship from the Deutsche Forschungsgemeinschaft (ME 3723/1-1, ME 3723/2-1); and SB was funded by a Deutsche Forschungsgemeinschaft grant (GZ:BH 155/1-1). SA was funded by the 2015 John M. Vierling, MD Postdoctoral Research Fellowship Award from the American Liver Foundation, the 2016 Innovation Award from the Cholangiocarcinoma Foundation, and by a 2017–2020 Research Scholar Award from the American Gastroenterological Association. AF was funded by a postdoctoral fellowship from the Recherche Médicale (SPE20170336778) and the 2018 Hans Popper Memorial Postdoctoral Research Fellowship Award from the American Liver Foundation. ES was funded by NIH grants R01DK085252 and P01CA233452. RK was funded by NIH grant P01CA117969. RW was funded by NIH grant 5U54CA193417. This study used resources of the Cancer Center Flow Core Facility, funded in part through NIH grant P30CA013696.

Address correspondence to: Robert F. Schwabe, 1130 St. Nicholas Avenue, ICRC 926, New York, New York 10032, USA. Phone: 212.851.5464; Email: rfs2102@cumc.columbia.edu. Or to: Ingmar Mederacke, Department of Gastroenterology, Hepatology, and Endocrinology, Hannover Medical School, Carl-Neuberg-Str. 1, Hannover D-30625, Germany. Phone: 49.511.532.6619. Email: mederacke.ingmar@mh-hannover.de.

1. Chiang AC, Massague J. Molecular basis of metastasis. *N Engl J Med*. 2008;359(26):2814–2823.
2. Griscom JT, Wolf PS, eds. Liver Metastasis. StatPearls Publishing; 2021.
3. Lambert AW, et al. Emerging biological principles of metastasis. *Cell*. 2017;168(4):670–691.
4. Nguyen DX, et al. Metastasis: from dissemination to organ-specific colonization. *Nat Rev Cancer*. 2009;9(4):274–284.
5. Mizrahi JD, et al. Pancreatic cancer. *Lancet*. 2020;395(10242):2008–2020.
6. Wolfgang CL, et al. Recent progress in pancreatic cancer. *CA Cancer J Clin*. 2013;63(5):318–348.
7. D'Angelica M, et al. Ninety-six five-year survivors after liver resection for metastatic colorectal cancer. *J Am Coll Surg*. 1997;185(6):554–549.
8. Tomlinson JS, et al. Actual 10-year survival after resection of colorectal liver metastases defines cure. *J Clin Oncol*. 2007;25(29):4575–4580.
9. Hanahan D, Coussens LM. Accessories to the crime: functions of cells recruited to the tumor microenvironment. *Cancer Cell*. 2012;21(3):309–322.
10. Quante M, et al. The gastrointestinal tumor

microenvironment. *Gastroenterology*. 2013;145(1):63–78.
11. Hessmann E, et al. Microenvironmental determinants of pancreatic cancer. *Physiol Rev*. 2020;100(4):1707–1751.
12. Biffi G, Tuveson DA. Diversity and biology of cancer-associated fibroblasts. *Physiol Rev*. 2021;101(1):147–176.
13. Erez N, et al. Cancer-associated fibroblasts are activated in incipient neoplasia to orchestrate tumor-promoting inflammation in an NF-kappaB-dependent manner. *Cancer Cell*. 2010;17(2):135–147.
14. Kalluri R. The biology and function of fibroblasts in cancer. *Nat Rev Cancer*. 2016;16(9):582–598.
15. Sahai E, et al. A framework for advancing our understanding of cancer-associated fibroblasts. *Nat Rev Cancer*. 2020;20(3):174–186.
16. Su S, et al. $CD10^+GPR77^+$ cancer-associated fibroblasts promote cancer formation and chemoresistance by sustaining cancer stemness. *Cell*. 2018;172(4):841–856.
17. Ozdemir BC, et al. Depletion of carcinoma-associated fibroblasts and fibrosis induces immunosuppression and accelerates pancreas cancer with reduced survival. *Cancer Cell*. 2014;25(6):719–734.
18. Rhim AD, et al. Stromal elements act to restrain, rather than support, pancreatic ductal adenocarcinoma. *Cancer Cell*. 2014;25(6):735–747.
19. Affo S, et al. The role of cancer-associated fibroblasts and fibrosis in liver cancer. *Annu Rev Pathol*. 2017;12:153–186.
20. Bissell MJ, Hines WC. Why don't we get more cancer? A proposed role of the microenvironment in restraining cancer progression. *Nat Med*. 2011;17(3):320–329.
21. Bartoschek M, et al. Spatially and functionally distinct subclasses of breast cancer-associated fibroblasts revealed by single cell RNA sequencing. *Nat Commun*. 2018;9(1):5150.
22. Elyada E, et al. Cross-species single-cell analysis of pancreatic ductal adenocarcinoma reveals antigen-presenting cancer-associated fibroblasts. *Cancer Discov*. 2019;9(8):1102–1123.
23. Kieffer Y, et al. Single-cell analysis reveals fibroblast clusters linked to immunotherapy resistance in cancer. *Cancer Discov*. 2020;10(9):1330–1351.
24. Chen X, Song E. Turning foes to friends: targeting cancer-associated fibroblasts. *Nat Rev Drug Discov*. 2019;18(2):99–115.
25. Costa-Silva B, et al. Pancreatic cancer exosomes initiate pre-metastatic niche formation in the liver. *Nat Cell Biol*. 2015;17(6):816–826.
26. Mederacke I, et al. Fate tracing reveals hepatic stellate cells as dominant contributors to liver fibrosis independent of its aetiology. *Nat Commun*. 2013;4:2823.
27. Levental KR, et al. Matrix crosslinking forces tumor progression by enhancing integrin signaling. *Cell*. 2009;139(5):891–906.
28. Northey JJ, et al. Tissue force programs cell fate and tumor aggression. *Cancer Discov*. 2017;7(11):1224–1237.
29. Barbazan J, Matic Vignjevic D. Cancer associated fibroblasts: is the force the path to the dark side? *Curr Opin Cell Biol*. 2019;56:71–79.
30. Iwaisako K, et al. Origin of myofibroblasts in the fibrotic liver in mice. *Proc Natl Acad Sci U S A*. 2014;111(32):E3297–E3305.
31. Ahmed M. Gastrointestinal neuroendocrine tumors in 2020. *World J Gastrointest Oncol*. 2020;12(8):791–807.
32. Laskaratos FM, et al. Neuroendocrine tumors and fibrosis: an unsolved mystery? *Cancer*. 2017;123(24):4770–4790.
33. Erkan M, et al. Organ-, inflammation- and cancer specific transcriptional fingerprints of pancreatic and hepatic stellate cells. *Mol Cancer*. 2010;9:88.
34. Ishaque N, et al. Whole genome sequencing puts forward hypotheses on metastasis evolution and therapy in colorectal cancer. *Nat Commun*. 2018;9(1):4782.
35. Shen Y, et al. Reduction of liver metastasis stiffness improves response to bevacizumab in metastatic colorectal cancer. *Cancer Cell*. 2020;37(6):800–817.
36. Efremova M, et al. CellPhoneDB: inferring cell-cell communication from combined expression of multi-subunit ligand-receptor complexes. *Nat Protoc*. 2020;15(4):1484–1506.
37. DeLeve LD. Liver sinusoidal endothelial cells in hepatic fibrosis. *Hepatology*. 2015;61(5):1740–1746.
38. Tang VW. Collagen, stiffness, and adhesion: the evolutionary basis of vertebrate mechanobiology. *Mol Biol Cell*. 2020;31(17):1823–1834.
39. Yang YM, et al. Hyaluronan synthase 2-mediated hyaluronan production mediates Notch1 activation and liver fibrosis. *Sci Transl Med*. 2019;11(496):eaat9284.
40. Ropponen K, et al. Tumor cell-associated hyaluronan as an unfavorable prognostic factor in colorectal cancer. *Cancer Res*. 1998;58(2):342–347.
41. Whatcott CJ, et al. Desmoplasia in primary tumors and metastatic lesions of pancreatic cancer. *Clin Cancer Res*. 2015;21(15):3561–3568.
42. Lee-Sayer SS, et al. The where, when, how, and why of hyaluronan binding by immune cells. *Front Immunol*. 2015;6:150.
43. Cyphert JM, et al. Size matters: molecular weight specificity of hyaluronan effects in cell biology. *Int J Cell Biol*. 2015;2015:563818.
44. Kamada N, et al. Reversal of transplantation immunity by liver grafting. *Nature*. 1981;292(5826):840–842.
45. Lang KS, et al. Immunoprivileged status of the liver is controlled by Toll-like receptor 3 signaling. *J Clin Invest*. 2006;116(9):2456–2463.
46. Ramanathan RK, et al. Phase IB/II randomized study of FOLFIRINOX plus pegylated recombinant human hyaluronidase versus FOLFIRINOX alone in patients with metastatic pancreatic adenocarcinoma: SWOG S1313. *J Clin Oncol*. 2019;37(13):1062–1069.
47. Shaked Y. The pro-tumorigenic host response to cancer therapies. *Nat Rev Cancer*. 2019;19(12):667–685.
48. Buchtler S, et al. Cellular origin and functional relevance of collagen I production in the kidney. *J Am Soc Nephrol*. 2018;29(7):1859–1873.
49. Phaneuf D, et al. Generation of a mouse expressing a conditional knockout of the hepatocyte growth factor gene: demonstration of impaired liver regeneration. *DNA Cell Biol*. 2004;23(9):592–603.
50. Soares KC, et al. A preclinical murine model of hepatic metastases. *J Vis Exp*. 2014(91):51677.